

# Extracting Information from AGN Variability

Vishal P. Kasliwal,<sup>1</sup>★ Michael S. Vogeley,<sup>1</sup> Gordon T. Richards,<sup>1</sup> Joshua Williams,<sup>2</sup> and Michael T. Carini<sup>2</sup>

<sup>1</sup>*Department of Physics, Drexel University, Philadelphia, PA 19104-2875, USA*

<sup>2</sup>*Department of Physics and Astronomy, Western Kentucky University, Bowling Green, KY 42101-1077, USA*

Accepted XXX. Received YYY; in original form ZZZ

## ABSTRACT

AGN exhibit rapid, high amplitude stochastic flux variability across the entire electromagnetic spectrum on timescales ranging from hours to years. The cause of this variability is poorly understood because of the complexity of the phenomenon being observed as well as a lack of a concrete picture of the physical configuration of the material accreting onto the central supermassive black hole. Therefore, variability is usually viewed as potentially useful for classification but no clear techniques exist to use variability to probe the physical conditions present in the nucleus of an AGN host galaxy. We present a framework for using variability to constrain the physical processes at work in the vicinity of the central engine. The variability observed in the AGN is interpreted in the mathematical context of a differential equation driven by a stochastic process. The Green's function of the differential equation quantifies the time-domain evolution of a perturbation in the observed flux and hence probes the physical processes at work in the material in-falling onto the central engine. The power spectral density of the stochastic process driving the differential equation characterizes the physical processes responsible for the perturbations in flux. We outline a method to recover the coefficients of the differential equation as well as the driving stochastic process from the noisy observed light curve and suggest extensions to multi-band data.

**Key words:** galaxies: active – galaxies: Seyfert – quasars: general – accretion, accretion discs

## 1 INTRODUCTION

Active Galactic Nuclei (AGN) exhibit variability on timescales ranging from minutes and hours to years over the full electromagnetic spectrum. The underlying cause of the variability is unknown though models range from local viscosity fluctuations to oscillatory modes in the accretion disk (Ulrich et al. 1997). AGN are powered by the accretion of matter onto a central supermassive black-hole (Rees 1984). Matter infalling onto the supermassive black-hole must lose angular momentum during in-spiral. The loss of angular momentum results in the conversion of gravitational binding energy to the kinetic energy of the flow. A portion of this kinetic energy is radiated away resulting in the characteristic appearance of the AGN high luminosity ( $\sim 10^{47}$  erg s<sup>-1</sup> for the brightest quasars) emanating from a small volume ( $\sim 10^{14}$  cm) of space (Edelson et al., 1996). The open questions are: (1) What is the angular momentum-loss mechanism responsible for creating an inward flow? and (2) What

is the process responsible for the highly efficient conversion of the kinetic energy of the accretion flow into radiation?

It is generally accepted that the accretion inflow results in the formation of an accretion disk (Koratkar & Blaes 1999; Pringle 1981). Atleast three mechanisms may be responsible for the extraction of angular momentum from the accretion flow in a standard disk: (1) Magnetorotational Instability (MRI) generated turbulence (Balbus & Hawley 1991; Hawley & Balbus 1991, 1992; Balbus & Hawley 1992; Hawley, Gammie & Balbus 1995)—see the excellent review in Balbus & Hawley (1997); (2) Large scale magnetohydrodynamic (MHD) outflow caused external stresses (Blandford & Payne 1982); and (3) Shocks produced by non-axisymmetric waves (Fragile & Blaes 2008). MRI prescriptions for angular momentum transport are succinctly quantified by the alpha-prescription of Shakura & Sunyaev (1973)—see Balbus & Papaloizou (1999). Under the alpha-prescription, accretion flows are modelled as solutions of the vertically integrated hydrodynamic equations for the conservation of mass, radial and angular momentum etc... Stability criteria then dictate that solutions be of one of three types as characterized by location in surface density-mass accretion rate phase space (Blaes 4). Low accretion rate coupled with low surface den-

\* E-mail: vpk24@drexel.edu

sity results in the formation of advection-dominated accretion flows (Narayan & Yi 1994, 1995a,b; Abramowicz et al. 1995; Chen et al. 1995) where the cooling time of the accretion flow is much greater than the infall time. Such disks are optically thin and may exist in low-luminosity AGN. Quasars, Seyfert 1s and the intermediate states of black-hole X-ray binaries (BHXRBS) are thought to possess radiation pressure dominated 'slim' disks ( $H/r < 1$  where  $H$  is the local disk height at radius  $r$ ) with medium surface mass densities and very high accretion rates (Abramowicz et al. 1988). Such disks also have shorter inflow time as compared to the cooling timescale making the flow advective. The third stable solution occurs at high surface mass density but low accretion rate and results in the formation of classic 'thin' accretion disks that are optically thick and geometrically thin ( $H/r \ll 1$ ) (Shakura & Sunyaev 1973; Frank, King & Raine 2002). These disks are probably prevalent in BHXRBS in the high and soft states and in some QSOs (Blaes 4).

Numerous mechanisms have been posited for producing variability in accretion disks (Done 2014; Maccarone 2014; Uttley & Casella 2014). While we are concerned primarily with accretion onto supermassive black holes (SMBH) in AGN, a fair fraction of the theory is developed with BHXRBS accretion in mind. While similarities exist between accretion in BHXRBS and AGN, the difference in energy densities is considerable with AGNs having considerably higher luminosities and exhibiting variability on longer timescales. For instance, quasi-periodic oscillations (QPO) are routinely observed in BHXRBS, whereas in AGN there few reports of QPOs (Gierliński et al. 2008; Grindlay et al. 2014). While BHXRBS are commonly observed to shift between various spectral states, such transitions have not been observed in AGN to date (Kelly et al. 2011).

AGN optical variability may arise due to fluctuations in the Shakura & Sunyaev (1973) viscosity parameter  $\alpha$ . Lyubarskii (1997) showed that local stochastic fluctuations in the accretion disk are capable of producing the power law PSDs observed in AGN and BHXRBS. Such fluctuation  thought to propagate inwards over time suggesting that a powerful observational test is the observation of blue-lags (Uttley & Casella 2014) i.e. light curve variations at shorter wavelengths lagging those at longer wavelengths. Evidence for the propagating fluctuation model was provided by Miyamoto et al. (1988) who observed that hard X-ray variations in Cyg X-1 lagged behind soft X-ray variations with an inverse scaling between the time lag and the variability timescale. Starling et al. (2004) used the viscosity fluctuation model to impose lower limit of  $\alpha \sim 0.01$  on the disk viscosity. A later study by King et al. (2007) using AGN variability triggered by viscosity fluctuations suggest that  $\alpha \sim 0.1\text{--}0.4$ . Wood et al. (2001) examined a variant of the Lyubarskii (1997) propagating fluctuations model in which episodic mass deposition at the outer edge of the accretion disk triggers viscosity fluctuations in the accretion disk that evolve via the standard non-linear diffusion equation for the surface mass density

$$\frac{\partial \Sigma}{\partial t} = \frac{3}{r} \frac{\partial}{\partial r} \left[ \sqrt{r} \frac{\partial (\nu \Sigma \sqrt{r})}{\partial r} \right], \quad (1)$$

where  $\nu = \alpha c_S H$  is the kinematic viscosity and  $\Sigma$  is the surface mass density (Pringle 1981; Frank et al. 2002). This

model was revisited by Titarchuk et al. (2007) who generalized the treatment of Wood et al. (2001) to include time-dependent fluctuation sources located randomly on the disk face. By applying the surface mass density equation (1), Titarchuk et al. (2007) follow the evolution of perturbations to the mass surface density and luminosity arising from viscosity that is a power-law function of disk radius. Subsequently, Kelly et al. (2011) studied solutions to the surface mass density equation perturbed by stochastic fluctuations and showed that the resulting light curve can be expressed as a linear combination of multiple Ornstein-Uhlenbeck processes (Kelly et al. 2009; Gillespie 1996).

Accretion disk variability may also be caused by the existence of 'hot-spots' in the accretion disk (Maccarone 2014). Hot spots are thought to arise when accretion streams impact the disk resulting in shock heating. Such hot spots have already been detected during periods of quiescence in BHXRBS Froning et al. (2011); McClintock et al. (1995). Alternatively, thermal viscous instabilities or a variable mass transfer rate may be responsible for accretion disk variability (Lasota 2001; Coriat et al. 2012), though the amplitude of the variability should be much smaller and the timescale much longer for AGN than for BHXRBS (Hameury et al. 2009).

Other sources of variability include magnetic flares in the corona of the accretion disk (Poutanen & Fabian 1999) or from the hot accretion flow itself (Veledina et al. 2013). Alternatively, dynamo processes due to the magnetic fields threading the disk may be responsible for producing variability (Livio et al. 2003; King et al. 2004; Mayer & Pringle 2006). Janiuk & Czerny (2007) have suggested that the variability may be produced in the hot X-ray corona surrounding the accretion disk from the evaporation of mass perturbations in the disk. Misra & Zdziarski (2008) suggested that the X-ray variability of Cyg X-1 can be modelled as a damped harmonic oscillator driven by noise. Quasi-periodic signals in the light curve may be produced by weak shocks in the innermost region of the accretion caused by the presence of a tilt in the accretion disk of the black hole (Fragile et al. 2007; Fragile & Blaes 2008). Alternatively, quasi-periodic signals may be caused by global oscillation modes or parametric resonance instability (Reynolds & Miller 2009; O'Neill et al. 2009, 2011). Variability may also be produced by standing shocks interacting with fluctuations in tilted accretion disks (Henisey et al. 2012).

Numerical simulations of light curves from accretion disks began appearing in the literature starting with Schnittman et al. (2006). A ray-tracing and radiative transfer code was used to create images of a simulated accretion disk. Using images generated during multiple time dumps in the simulation, Schnittman et al. (2006) were able to create mock light curves resulting from accretion flows. Noble & Krolik (2009) performed fully General-Relativistic (GR) magnetohydrodynamic (MHD) simulations of accretion flows around black holes and showed that while the variability was generated by accretion rate variances caused by MHD turbulence, time delay effects steepened the PSD of the variations. Other GRMHD simulations have also shown that MHD turbulence results in accretion rate variations that can produce variability (Mościbrodzka et al. 2009; Dexter et al. 2009, 2010). Recently, Schnittman & Krolik (2013) and Schnittman et al. (2013) have even managed to produce

full (X-ray) spectra demonstrating the effect of variability on the spectral slope.

 Several mechanisms may be responsible for the variability observed in AGN light curves. Light curves in the optical are driven by X-ray variability on shorter timescales but exhibit a local source of variability on longer timescales. In this paper, we propose a method for analyzing observed light curves, particularly in the UV through IR where the fluctuations are smaller, that facilitates comparison with analytic and simulation work on variability. Our method builds on the Continuous-time AutoRegressive Moving Average (C-ARMA) modelling technique of Kelly et al. (2014) but proposes to view the C-ARMA equation as being representative of the physics governing variability i.e. the C-ARMA process-like behavior is a direct result of the physics driving the variability. In section 2, we show that linearization of a non-linear equation such as the surface mass density equation of (1) that governs how perturbations evolve results in a driven-linear differential equation. In the following section we suggest that the Green's function of the linearized differential equation be used to probe dissipation physics in the accretion disk. Section 4 proposes a form for the disturbances driving the flux perturbations-colored noise stochastic processes. A simple example of a C-ARMA process—the C-ARMA(2,1) process—is presented in section 5. Sections 6 through 9 present details of inferring the properties of the C-ARMA process from noisy observations using the Kalman filter. We end with an example of the application of C-ARMA modelling to the *Kepler* light curve of the Seyfert 1 galaxy Zw 229-15 in which we demonstrate how the C-ARMA model can be used to explain the multiple slopes and timescales found in the light curve of this AGN by previous work.

## 2 HOW DO FLUX PERTURBATIONS EVOLVE?

 Let the total flux emitted by an AGN be  $F(t)$ . Suppose  $F$  obeys the  $p^{\text{th}}$ -order non-linear differential equation

$$\frac{d^p F}{dt^p} = g(F, \frac{dF}{dt}, \dots, \frac{d^{p-1}F}{dt^{p-1}}, \mathcal{F}, t), \quad (2)$$

where  $\mathcal{F}$  is the contribution to the total flux from the appearance of hot- and cold-spots in the accretion disk. We shall attempt to linearize this system by probing the behavior of a small perturbation in flux about a solution to this equation (Wiberg 1971; Stengel 1994). We begin by rewriting this  $n^{\text{th}}$ -order non-linear differential equation for  $F(t)$  as a series of coupled 1<sup>st</sup>-order non-linear differential equations for  $F(t)$  and its derivatives. Define

$$F_k(t) = \frac{d^{k-1}F(t)}{dt^{k-1}}, \quad (3)$$

for  $1 \leq k \leq n$ . Since

$$\frac{dF_k}{dt} = \frac{d}{dt} \left( \frac{d^{k-1}F}{dt^{k-1}} \right) = \frac{d^k F}{dt^k} = F_{k+1}, \quad (4)$$

we have

$$\begin{aligned} \frac{dF_1}{dt} &= F_2, \\ &\vdots \\ \frac{dF_{p-1}}{dt} &= F_p. \end{aligned} \quad (5)$$

Then, we may rewrite equation (2) as

$$\frac{dF_p}{dt} = g(F_1, F_2, \dots, F_p, \mathcal{F}, t). \quad (6)$$

To simplify further analyses  shall linearize this system of equations by looking at the terms of the equations in the presence of a small perturbation. Suppose that starting from initial conditions  $F_1(t_0), \dots, F_p(t_0)$  with input contributions  $\mathcal{F}_0(t)$ , our system evolves as per the solutions  $\phi_1(t), \dots, \phi_p(t)$  i.e. these solutions obey equation (6) under the constraints of equation (5). Now consider the evolution of the system starting from the (slightly perturbed) initial conditions  $F'_1(t_0) = F_1(t_0) + X_1(t_0), \dots, F'_p(t_0) = F_p(t_0) + X_p(t_0)$  where the various  $X_k$  are small. Furthermore, we shall also subject the system to a slightly perturbed input  $\mathcal{F}'_0(t) = \mathcal{F}_0(t) + X_0(t)$ . Then the perturbed solutions,  $\chi_1(t), \dots, \chi_p(t)$ , must continue to satisfy equation (6) under the constraints of equation (5). Starting with the constraints, we have

$$\begin{aligned} \frac{d(\phi_1 + \chi_1)}{dt} &= \frac{d\phi_1}{dt} + \frac{d\chi_1}{dt} = \phi_2 + \chi_2, \\ &\vdots \\ \frac{d(\phi_{p-1} + \chi_{p-1})}{dt} &= \frac{d\phi_{p-1}}{dt} + \frac{d\chi_{p-1}}{dt} = \phi_p + \chi_p, \end{aligned} \quad (7)$$

But since the  $\phi_k$  satisfy equation (5), we have

$$\begin{aligned} \frac{d\chi_1}{dt} &= \chi_2, \\ &\vdots \\ \frac{d\chi_{p-1}}{dt} &= \chi_p. \end{aligned} \quad (8)$$

To linearize equation (6), we begin by noting

$$\frac{d(\phi_p + \chi_p)}{dt} = \frac{d\phi_p}{dt} + \frac{d\chi_p}{dt} = g(F'_1, F'_2, \dots, F'_p, \mathcal{F}'_0, t). \quad (9)$$

We may Taylor expand the RHS of this equation about the  $\phi_1, \dots, \phi_p$  and  $\mathcal{F}_0$  and cancel  $d\phi_p/dt = f(\phi_1, \phi_2, \dots, \phi_p, \mathcal{F}_0, t)$  to obtain

$$\frac{d\chi_p}{dt} = \left. \frac{\partial g}{\partial F_1} \right|_{\phi_1} \chi_1 + \dots + \left. \frac{\partial g}{\partial F_p} \right|_{\phi_p} \chi_p + \left. \frac{\partial g}{\partial \mathcal{F}_0} \right|_{\mathcal{F}_0} \mathcal{F}'_0. \quad (10)$$

Equations (8) and (10) are the linearized, 1<sup>st</sup> system of equations that describe the evolution of a tiny perturbation of the flux about an exact solution. In general, the coefficients of the  $\chi_k$  in equation (10) are functions of time and change as the system evolves. Let us consider the special case where the exact solution is the steady-state solution (if it exists). Under this restriction, equation (10) governing the evolution of a tiny perturbation in the flux simplifies to

$$\frac{d\chi_p}{dt} = a_1 \chi_1 + a_2 \chi_2 + \dots + a_n \chi_p + b \mathcal{F}'_0, \quad (11)$$

where

$$a_k = \frac{\partial g}{\partial F_k} \Big|_{\phi_k}, \quad (12)$$

and

$$b = \frac{\partial g}{\partial F_0} \Big|_{F_0}. \quad (13)$$

Therefore, we may re-write the linearized system of equations in equation (11) along with the constraints in equation (8) in the form of the  $n^{\text{th}}$ -order linear differential equation

$$\frac{d^p \chi}{dt^p} + \alpha_1 \frac{d^{p-1} \chi}{dt^{p-1}} + \dots + \alpha_{p-1} \frac{d \chi}{dt} + \alpha_p \chi = u, \quad (14)$$

where we have set  $\alpha_k = -a_k$  and  $u = bF'_0$  for brevity. Using differentials, this equation may be written as

$$d^p \chi + \alpha_1 d^{p-1} \chi + \dots + \alpha_{p-1} d \chi + \alpha_p \chi = u, \quad (15)$$

where  $du$  is an increment of  $u$ . Dimensional consistency requires that

$$[\alpha_k] = T^{-k}. \quad (16)$$

Since equation (14) governs how flux perturbations evolve over time, we shall refer to this equation as the ‘Dissipation Equation’. We define the characteristic polynomial of the LHS of this equation as

$$\alpha(z) = z^p + \alpha_1 z^{p-1} + \dots + \alpha_{p-1} z + \alpha_p, \quad (17)$$

with roots  $\rho_k$ . The flux perturbations are stable, i.e. do not increase without bound, if  $\text{Re}(\rho_k) < 0$ . We shall posit a form for  $u$  in section 4. In the next section, we present a convenient physical interpretation of equation (14) using the method of the Green’s function.



### 3 WHAT DOES THE DISSIPATION EQUATION TELL US ABOUT ACCRETION PHYSICS?

We propose that equation (14), the Dissipation Equation, be interpreted literally—we view it as characterizing the dissipative forces at work in the accretion disk. We can understand how accretion physics works by studying the Green’s function of this equation (Pandit & Wu 2001) and comparing it to the expected behavior of perturbations. Conceptually, the Green’s function of a system characterizes the impulse response of the system—particular solutions are found by linear superposition (integration) of the Green’s function over all the impulses that drive the system.

We compute the Green’s function equation (14) by finding a solution of the homogenized version of the equation. Consider the homogenous differential equation corresponding to equation (14)

$$\frac{d^p f}{dt^p} + \alpha_1 \frac{d^{p-1} f}{dt^{p-1}} + \dots + \alpha_{p-1} \frac{df}{dt} + \alpha_p f = 0. \quad (18)$$

To obtain the Green’s function solution of this equation, we shall drive this equation with a unit impulse, i.e. a Dirac delta function, located at the origin

$$\frac{d^p G}{dt^p} + \alpha_1 \frac{d^{p-1} G}{dt^{p-1}} + \dots + \alpha_{p-1} \frac{dG}{dt} + \alpha_p G = \delta(t), \quad (19)$$

where  $G(t)$  is the desired Green’s function solution. To find this solution, we shall first solve equation (18) by finding the roots of the characteristic polynomial of equation (17) and then apply boundary conditions based on the properties of  $\delta(x)$ . From the definition of the characteristic polynomial in equation (17), the (distinct) roots are  $\rho_k$  with  $\text{Re}(\rho_k) < 0$  for stability. Then the solution of the homogenous equation (18) is

$$f(t) = \sum_{k=1}^n c_k e^{\rho_k t}, \quad (20)$$

where the  $c_k$  are constants. Hence the solution of the nonhomogenous equation (19) may be found by using the continuity properties of  $G(t)$  and its derivatives. For  $t < 0$ ,  $d^{p-k} G/dt^{p-k} = 0$  for  $1 \leq k < p$  while at  $t = 0$ ,  $d^p G/dt^p$  has the same type of discontinuity as  $\delta(t)$ . Therefore  $d^{p-1} G/dt^{p-1} = 1$  when  $t = 0$ , i.e. it behaves like the step function. Next, we have that  $d^{p-k} G/dt^{p-k} = 0$  at  $t = 0$  for all  $1 < k \leq p$  since each successive lower-order derivative is a  $(k-1)^{\text{th}}$ -order polynomial located at the origin. Following this line of reasoning, we arrive at the following boundary conditions

$$\frac{d^{p-1} G}{dt^{p-1}} \Big|_{t=0} = 1, \quad (21)$$

and

$$\frac{d^{p-k} G}{dt^{p-k}} \Big|_{t=0} = 0, \quad (22)$$

for all  $2 \leq k \leq p$ . Computation of the derivatives in equations (21) and (22) results in

$$\sum_{k=1}^p c_k \rho_k^{p-1} = 1, \quad (23)$$

and

$$\sum_{k=1}^p c_k \rho_k^{k-1} = 0, \quad (24)$$

for all  $2 \leq k \leq p$ . The  $c_k$  may then be found by solving the matrix equation

$$\begin{pmatrix} \rho_1^{p-1} & \rho_2^{p-1} & \dots & \rho_{p-1}^{p-1} & \rho_p^{p-1} \\ \rho_1^{p-2} & \rho_2^{p-2} & \dots & \rho_{p-1}^{p-2} & \rho_p^{p-2} \\ \vdots & \vdots & \ddots & \vdots & \vdots \\ \rho_1 & \rho_2 & \dots & \rho_{p-1} & \rho_p \\ 1 & 1 & \dots & 1 & 1 \end{pmatrix} \begin{pmatrix} c_1 \\ c_2 \\ \vdots \\ c_{p-1} \\ c_p \end{pmatrix} = \begin{pmatrix} 1 \\ 0 \\ \vdots \\ 0 \\ 0 \end{pmatrix}. \quad (25)$$

To summarize, the Green’s function for equation (14) is given by

$$G(t) = \sum_{k=1}^p c_k e^{\rho_k t}, \quad (26)$$

where the  $c_k$  satisfy equation (25).

#### 4 WHAT CAUSES THE PERTURBATIONS?

The cause of perturbations, i.e. variability, in the flux emanating from an AGN is unknown, but we may construct a very-general mathematical model for the form of the flux perturbations based on physical and statistical arguments. The region of space surrounding the central engine is vast. The inner edge of the accretion disk is thought to begin a few  $r_G \sim 20$  AU ( $M_{BH} = 10^9 M_\odot$ ) away from the event-horizon, while the outer edge is thought to lie at a distance of a few parsec away from the event horizon. Contributions to the deviations in the flux most likely simultaneously arise from many individual locations in this system. Under the assumption that the distribution of energy released by each individual event is drawn from a distribution with finite second-moment, the central-limit-theorem assures us that the total energy introduced into the system at any instant will be drawn from a normal distribution i.e. some form of noise. Due to the non-linearity of the physics involved, it is quite likely that correlations exist between the energy released into the disk at different moments in time. Therefore, we shall model the correlations by treating the driving process  $u$  in equation (14) as a Gaussian process i.e. colored noise. Fundamental to the treatment of  $u$  as some form of noise process is the concept of Brownian motion, also known as the Wiener process  $W$  (Doob 1990; Davis 2002; Jacobs 2010; Øksendal 2014). The Wiener process cannot be used directly as the driving process because it is not stationary i.e. the likelihood of a given value of the Wiener process is time-dependent. This is because the power spectral density (PSD) of the Wiener process decreases as the square of the frequency and so has excess power on long timescales. A better choice for the driving process is some linear combination of the derivatives of  $W$ . Mathematically, due to the discontinuous nature of  $W$ , the derivatives of  $W$  are undefined. Instead, we shall use differentials

$$u = \beta_1 d^{p-1}(dW) + \beta_2 d^{p-2}(dW) + \dots + \beta_{p-1} d(dW) + \beta_p (dW), \quad (27)$$

where  $dW$  is the increment of the Wiener process and is well-defined. By definition

$$W(t) = \int_0^t dW. \quad (28)$$

Dimensional consistency requires that

$$[\beta_k] = [\chi] T^{\frac{1}{2}-k}, \quad (29)$$

where  $\chi$  is in units of flux, e.g. erg cm<sup>-2</sup>. Analogous to equation (17), we define the characteristic polynomial of equation (27) to be

$$\beta(z) = \beta_1 z^{p-1} + \beta_2 z^{p-2} + \dots + \beta_{p-1} z + \beta_p, \quad (30)$$

with roots  $\mu_k$ . For equation (27) to be invertible, we require that  $\text{Re}(\mu_k) < 0$ .

The PSD,  $S_{uu}(v)$ , of the process  $u(t)$  is defined to be

$$S_{uu}(v) = \langle |u(v)|^2 \rangle, \quad (31)$$

where

$$\tilde{u}(v) = \frac{1}{2\pi} \int_{-\infty}^{\infty} u(t) e^{-2\pi i v t} dt \quad (32)$$

is the Fourier transform of  $u(t)$ . The PSD of the Wiener

increments is constant at all frequencies (Brockwell 2001) i.e.

$$S_{dWdW} = \frac{1}{2\pi}, \quad (33)$$

corresponds to infinite total power when integrated over all frequencies. Real processes only resemble the Wiener process and Wiener increments over an interval of frequencies known as the bandpass of the process—outside this bandpass, the PSD is set to 0. The PSD of the driving process in equation (27) may be computed using

$$\widetilde{d^k u} = (2\pi i v)^k \tilde{u}, \quad (34)$$

in conjunction with equation (33) yielding

$$S_{uu}(v) = \frac{1}{2\pi} \sum_{j=1}^p \sum_{k=1}^p \beta_j \beta_k (2\pi i v)^{p-j} (-2\pi i v)^{p-k}, \quad (35)$$

which is a polynomial in  $v$ . This implies that at high frequencies, the power contributed by this process is unbounded. However, consider what happens to the PSD when  $dW$  is integrated— $S_{WW} \propto 1/v^2$ . Successive integrations decrease the logarithmic slope of the PSD at high frequencies by a factor of 2 each time. If  $u$  is supplied as input to equation (14), it is integrated  $n$ -times. If the overall process  $\chi$  is to have finite power at high frequencies, we must limit the highest-order of the derivative of  $dW$  in equation (27) to  $p-1$  so that after  $p$ -integrations, the overall process has PSD with negative logarithmic slope corresponding to finite high-frequency power i.e. the bandpass of the driving disturbance process rapidly decreases at high frequencies. At low frequencies, we expect the power in our system to drop to 0 as we approach the timescale on which AGN are active  $\sim 10^7$  yr. On the more relevant timescales that can be probed by us, the PSD should essentially flatten to a constant at low frequencies. Finally, we may formulate our system by combining equations (15) and (27) into the Itô differential equation

$$d^p \chi + \alpha_1 d^{p-1} \chi + \dots + \alpha_{p-1} d\chi + \alpha_p \chi = \beta_1 d^{p-1}(dW) + \dots + \beta_p (dW), \quad (36)$$

with  $\text{Re}(\rho_k) < 0$  and  $\text{Re}(\mu_k) < 0$  where the  $\rho_k$  and  $\mu_k$  are the roots of the autoregressive- and moving average- polynomials of equations (17) and (30) respectively. Given the form of the C-ARMA process, we can write the PSD of the C-ARMA process (Brockwell 2001) as

$$S_{\chi\chi}(v) = \frac{1}{2\pi} \frac{|\beta(2\pi i v)|^2}{|\alpha(2\pi i v)|^2}. \quad (37)$$

In practice not all of the  $\beta_k$  may be present. In particular, if the first  $k$  values of  $\beta_k = 0$ , the RHS has just  $q = p-k$  terms. A stochastic processes of this form is known in the statistical inferencing community as a *Continuous-time AutoRegressive Moving Average* process of order  $p$  and  $q$  or C-ARMA( $p,q$ ) process (Brockwell 2014, 2001, 1994; Kelly et al. 2014).

Fitting the observed light curve of an AGN to the CARMA process of equation (36) tells us how flux perturbations evolve via equations (26) and (25) and what the statistical properties of the driving noise process are via equation (35). These two functions may be matched to theoretical results about accretion disk instabilities in order to probe accretion physics.

## 5 C-ARMA MODELS IN PRACTICE: THE C-ARMA(2,1) PROCESS

We shall discuss the C-ARMA(2,1) process in detail because it has strong physical motivations and is relatively simple to interpret. Notice that in the process of linearizing the original non-linear differential equation of equation (2), we have not changed the order of the highest derivative of the flux that appears in that equation i.e. if the original equation governing the flux emitted by the accretion disk is of  $p^{\text{th}}$ -order, the corresponding linearized C-ARMA process is also of  $p^{\text{th}}$ -order. Most physical phenomenon are governed by 2<sup>nd</sup>-order equations. Hence, we may expect to find that in the linear regime, AGN variability is a C-ARMA(2, $q$ ) process with  $q < 2$ .

The general form of the C-ARMA(2, $q$ ) process is

$$d^2\chi + \alpha_1 d\chi + \alpha_2 \chi = \beta_1 d(dW) + \beta_2 (dW), \quad (38)$$

where  $[\alpha_1] = T^{-1}$ ,  $[\alpha_2] = T^{-2}$ ,  $[\beta_1] = [\chi] T^{-1/2}$ , and  $[\beta_2] = [\chi] T^{-3/2}$ . We identify equation (38) to be of the form of a *Damped Harmonic Oscillator* (DHO) that is driven by a colored noise process. We may identify  $\alpha_2$  with  $\omega^2$ , the angular frequency of the HO, and  $\alpha_1$  with  $2\omega\zeta_{\text{dHO}}$  where  $\zeta_{\text{dHO}}$  is the damping ratio (Pandit & Wu 2001, see chapter 7 for notation). From the angular frequency, we can calculate the time-period of the harmonic oscillator in the absence of damping  $T_{\text{HO}} = 2\pi/\omega$ . The roots of the LHS of equation (38) are given by

$$\rho_1, \rho_2 = -\omega\zeta_{\text{dHO}} \pm \omega\sqrt{\zeta_{\text{dHO}}^2 - 1}. \quad (39)$$

The behavior of the flux perturbations is nonphysical if  $\zeta_{\text{dHO}} = 0$ . For  $0 < \zeta_{\text{dHO}} < 1$ , the flux perturbations will oscillate in value around the steady-state flux value with angular frequency  $\omega' = \omega\sqrt{1 - \zeta_{\text{dHO}}^2}$  but gradually decrease in amplitude. If  $\zeta_{\text{dHO}} = 1$ , flux perturbations will rapidly die down to the steady-state flux, while if  $\zeta_{\text{dHO}} > 1$ , flux perturbations exponentially decay to the steady-state flux with the rate of decay increasing with  $\zeta_{\text{dHO}}$ . From equation (37), the PSD of the C-ARMA(2,1) process is given by

$$S_{\chi\chi}(v) = \frac{1}{2\pi} \frac{4\pi^2\beta_1^2 v^2 + \beta_2^2}{16\pi^4 v^4 + 4\pi^2(\alpha_1^2 - 2\alpha_2)v^2 + \alpha_2^2}, \quad (40)$$

which has frequency dependent behavior. At very high frequencies, the  $v^4$  term in the denominator will dominate whereas as lower frequencies, the PSD will look like the damped random walk PSD of Kelly et al. (2009) with  $S_{\chi\chi} \sim 1/v^2$ . At the lowest frequencies, we expect the PSD to be dominated by the frequency independent terms and asymptotically approach  $\beta_2^2/2\pi\alpha_2^2$ .

The Green's function of the DHO is given by

$$G(t) = \frac{e^{\rho_1 t} - e^{\rho_2 t}}{\rho_1 - \rho_2}, \quad (41)$$

where  $\rho_1$  and  $\rho_2$  are the roots of the autoregressive characteristic polynomial of equation (39). If  $\zeta_{\text{dHO}} > 1$  i.e. flux perturbations are constrained to be damped out by the dissipative processes in the accretion disk, then the roots are purely real-valued. A perturbation to the accretion disk flux in the form of an impulse at  $t = t_0$  will result in the flux increasing from  $t_0$  to  $t_{\max}$  given by

$$t_{\max} = \frac{1}{\rho_2 - \rho_1} \ln \left| \frac{\rho_1}{\rho_2} \right|. \quad (42)$$

After  $t_{\max}$ , the effect of the original perturbation decays to the steady-state flux level. Although the decay is not a pure exponential, it is useful to characterize the decay rate by an e-folding timescale  $t_{\text{e-fold}}$ . It may be computed by solving

$$G(t_{\text{e-fold}}) = \frac{G(t_{\max})}{e}, \quad (43)$$

numerically for  $t_{\text{e-fold}}$ .

In the case of the C-ARMA(2,1) process, the driving noise is best interpreted as the ‘acceleration’ of flux perturbations away from the steady-state flux level. The PSD of the driving noise process is given by

$$S_{uu}(v) = \frac{1}{2\pi} (4\pi^2\beta_1^2 v^2 + \beta_2^2). \quad (44)$$

At low frequencies, the  $\beta_2^2$  term in the RHS dominates i.e. the log-PSD slope is 0. At high frequencies, the  $4\pi^2\beta_1^2 v^2$  term drives the log-PSD slope to 2. The transition from the  $\beta_2^2$ -dominated to the  $4\pi^2\beta_1^2 v^2$ -dominated behavior occurs at

$$t_{\text{turn}} = \frac{2\pi\beta_1}{\beta_2}, \quad (45)$$

which may have physical significance in accretion physics. 

We shall now discuss how to infer the values of the co-efficients in the C-ARMA process describing accretion disk fluctuations in an AGN from observations of the light curve of the object.

## 6 FITTING A C-ARMA PROCESS TO OBSERVATIONS OF A LIGHT CURVE

We wish to infer the values of the co-efficients in equation (36) that defines C-ARMA in order to compute the physically interesting Green’s function and driving disturbance PSD for the observed light curve. Many techniques can be applied to perform this task. The most straightforward method of fitting a C-ARMA process to a light curve is by direct estimation of the PSD of the observed light curve. Using periodogram estimators of the PSD, the observed PSD can be compared PSD of equation (37) which is of the form of a rational function of  $v$ . This rational function form for the C-ARMA PSD allows it great flexibility in matching any observed PSD. This is the method advocated in Uttley, McHardy & Papadakis (2002).

We can also estimate the *Auto-Covariance Function* (ACF) of the observed light curve and fit it to the theoretical ACF of the C-ARMA process. From Brockwell (2001), we have

$$\gamma_{\chi\chi}(T) = \sum_{k=1}^p \frac{\beta(\rho_k)\beta(-\rho_k)}{\alpha(\rho_k)\alpha(-\rho_k)} e^{\rho_k T}, \quad (46)$$

where the  $\rho$  are the roots of the autoregressive characteristic polynomial. Following Kasliwal, Vogeley & Richards (2015b), we may fit estimates of the *Structure Function* (SF) of the observed light curve to the theoretical SF computed either directly from the C-ARMA ACF, or from Monte-Carlo simulations of light curves generated using the C-ARMA PSD of equation (37). 

The principle drawback with the methods above is that while we have expressions for the analytic forms of the PSD, ACF, and SF of the C-ARMA process, we have no results

about the *distributions* of the estimates of these statistics about the theoretical curve (Brockwell & Davis 2010). In fact, as shown in Emmanoulopoulos, McHardy & Uttley (2010) and in Kasliwal et al. (2015b), it is the estimates of the logarithm of the SF rather than the SF that are Gaussian distributed. This means that the application of the methods above relies on Monte-Carlo techniques to estimate the distribution of the property, be it PSD, ACF or Sf, being fit. Usually, some assumption of normality is made and typically the estimates are treated as independent purely for computational practicality.

Alternatively, one may use the maximum-likelihood methods of Rybicki & Press (1992, 1995) and Kozlowski et al. (2010) along with the prescription for the ACF given in equation (46) to obtain the best-fit CARMA parameters. As shown in Hamilton (1994), the Press-Rybicki-Hewitt (PRH) procedure provides maximum likelihood estimates of model parameters assuming that the light curve is a Gaussian process. It is mathematically equivalent to using a Kalman filter to compute the likelihood of the light curve given the C-ARMA model. However, while the PRH method operates on all the light curve measurements simultaneously and requires computation of the determinant and inverse of matrices that have dimensions identical to the length of the light curve in number of observations. The Kalman filter, on the other hand, requires trivial matrix inversions and determinant calculations ( $1 \times 1$  matrices) because it operates on the light curve observation-by-observation. An added advantage of the Kalman filter is that it is designed to allow us to update the likelihood calculation when new measurements become available as opposed to the PRH formulation in which the likelihood has to be re-computed from scratch. The framework in which the Kalman filter operates, the state-space framework, is also easy to extend to the case of multi-band, non-simultaneous observations of AGN as will become available with next generation surveys such as PanSTARRS and the LSST.



## 7 STATE SPACE REPRESENTATION OF A C-ARMA PROCESS

We shall use the Kalman filter (Kalman 1960; Simon 2006) to obtain Bayesian posteriors for the distribution function of the C-ARMA coefficients. Application of the Kalman filter requires that the system represented in *state-space* form. Inferencing via the Kalman filter using a state-space representations has been successfully applied to control complex systems including the Apollo program for over 50 years (Grewal & Andrews 2010), and has since then come into vogue in fields as diverse as biostatistics (Jones 1993) and econometrics (Durbin & Koopman 2012; Harvey 1991).

The central concept underlying the application of the Kalman filter is that of the state of the system—an abstract quantity that completely characterizes the system at a given instant e.g. the position and velocity of a rocket. This state evolves via the state-equation—a differential (continuous-time) or difference (discrete-time) equation that tells us how to update the state of the system from time-step to time-step. Generically, the state-equation consists of three components—(1) a deterministic isolated time evolution component; (2) a deterministic input response component; and

(3) a random disturbance component. The input component can be used to *control* the system by driving it to a desired state. One of the key benefits of the Kalman approach is that the state is not observed directly—instead the system is monitored via the observation equation e.g. we observe the angular position of the rocket. The act of observation is necessarily imprecise and hence the observed quantities are contaminated with noise. The Kalman filter is used to recover estimates of the state of the system given the noisy observations of the state and the form of the state- and observation-equations.

A dichotomy exists between the application of the Kalman filter in the fields of control systems engineering v/s econometrics and biostatistics. Typically, in control systems engineering, the numerical forms of state- and observation-equations are known and the Kalman filter is used to estimate the system-state in real time with the view of estimating the best input to drive the system to the desired state i.e. closed loop control. In the fields of biostatistics and econometrics, the numerical forms of the state- and observation-equations are unknown and the Kalman filter is used to estimate the *likelihood* of the numerical coefficients in the state- and observation-equations (Simon 2006) given the observed data. The likelihood computations may then be used to either simply optimize the C-ARMA process parameters or, better yet, obtain the full likelihood distribution of the C-ARMA process parameters conditioned on the data. It is *this usage* that concerns us here.

We shall represent the C-ARMA process in continuous-time state-space form (Wiberg 1971; Friedland 2005) as

$$\dot{\mathbf{x}} = \mathbf{A}\mathbf{x}dt + \mathbf{B}dw, \quad (47)$$

and

$$\chi(t) = \mathbf{H}(\mathbf{t})\mathbf{x} + v, \quad (48)$$

where  $\mathbf{x}$  is the system-state vector,  $W$  is the Wiener process of section 4,  $v \sim \mathcal{N}(0, \sigma_N^2)$  is the measurement noise, and  $\chi$  is the (noisy) observed flux at time  $t$ . The matrix  $\mathbf{A}$  is known as the ‘state-transition matrix’, while the matrix  $\mathbf{H}$  is known as the ‘observation matrix’. There are infinitely many ways of writing a C-ARMA process in state-space form—we shall discuss the 2 most relevant (Denham 1974; Dickinson et al. 1974). All other forms may be obtained from these ‘canonical’ forms via similarity transforms.

The ‘1<sup>st</sup> canonical form’ of Wiberg (1971) which is also the ‘2<sup>nd</sup> companion form’ of Friedland (2005), puts the dynamics of the C-ARMA process solely into the state-equation by representing equation (36) using

$$\mathbf{A} = \begin{pmatrix} -\alpha_1 & 1 & \dots & 0 & 0 \\ -\alpha_2 & 0 & \dots & 0 & 0 \\ \vdots & \vdots & \ddots & \vdots & \vdots \\ -\alpha_{p-1} & 0 & \dots & 0 & 1 \\ -\alpha_p & 0 & \dots & 0 & 0 \end{pmatrix}; \quad \mathbf{B} = \begin{pmatrix} \beta_1 \\ \beta_2 \\ \vdots \\ \beta_{p-1} \\ \beta_p \end{pmatrix}; \quad \mathbf{H} = \begin{pmatrix} 1 \\ 0 \\ \vdots \\ 0 \\ 0 \end{pmatrix}^\top. \quad (49)$$

The ‘2<sup>nd</sup> canonical form’ or ‘phase-variable canonical

form of Wiberg (1971) which is the ‘1<sup>st</sup> companion form’ of Friedland (2005) (see also Kelly et al. (2014) and references therein), breaks-up the dynamics of the C-ARMA process across the state- and observation-equations by representing equation (36) using

$$\mathbf{A} = \begin{pmatrix} 0 & 1 & 0 & \dots & 0 \\ 0 & 0 & 1 & \dots & 0 \\ \vdots & \vdots & \vdots & \ddots & \vdots \\ 0 & 0 & 0 & \dots & 1 \\ -\alpha_p & -\alpha_{p-1} & -\alpha_{p-2} & \dots & -\alpha_1 \end{pmatrix};$$

$$\mathbf{B} = \begin{pmatrix} 0 \\ 0 \\ \vdots \\ 0 \\ 1 \end{pmatrix}; \mathbf{H} = \begin{pmatrix} \beta_p \\ \beta_{p-1} \\ \vdots \\ \beta_2 \\ \beta_1 \end{pmatrix}^\top. \quad (50)$$

Note that the components of the state-vector  $\mathbf{x}$  are not the same in the two representations but carry the same information i.e. we are projecting the abstract state-vector into a particular coordinate system. Regardless of the choice of representations used, we can integrate the state-equation (Brockwell 1994; Øksendal 2014) to obtain an update equation for  $\mathbf{x}$

$$\mathbf{x}(t + \delta t) = \mathbf{x}(t) e^{\mathbf{A}\delta t} + \int_0^{\delta t} e^{\mathbf{A}(\delta t-u)} \mathbf{B} dW, \quad (51)$$

where  $\int_0^{\delta t} e^{\mathbf{A}(\delta t-u)} \mathbf{B} dW$  is an Itô integral. The presence of the stochastic Itô integral implies that we cannot predict *exactly* what the future values of  $\mathbf{x}$  will be because the integral in equation (51) contributes randomly for every realization of the process. However, we can predict the expectation value of the integral and the  $1 - \sigma$  confidence limit on that expectation value (Davis 2002, chapter 6). These are given by

$$\left\langle \int_0^{\delta t} e^{\mathbf{A}(\delta t-u)} \mathbf{B} dW \right\rangle = 0, \quad (52)$$

and

$$\left\langle \int_0^{\delta t} e^{\mathbf{A}(\delta t-u)} \mathbf{B} dW \int_0^{\delta t} e^{\mathbf{A}(\delta t-u)} \mathbf{B} dW \right\rangle =$$

$$\int_0^{\delta t} e^{\mathbf{A}\xi} \mathbf{B} \mathbf{B}^\top e^{\mathbf{A}^\top \xi} d\xi. \quad (53)$$

Observation patterns can be broadly classified into two groups - those with regular sampling (RS) and those with irregular sampling (IRS). RS patterns occur when observations are made at fixed intervals to within the precision of the clock governing the schedule. We can relate the number of observations  $N$  made to the duration of the sampling  $T$  in terms of the sampling interval  $\delta t = T/N$ . The times at which the process is sampled  $t$  must then be given by  $t = n\delta t$  for  $1 \leq n \leq N$  and can therefore be indexed by  $n$ . Occasionally, natural or mission-induced events make it impossible to observe the object of interest for one or more simultaneous cadences. Such incidents are called ‘missing-observations’. We track missing-observations via a mask  $\mathcal{M}_n$ . If the  $n^{\text{th}}$  observation is missing,  $\mathcal{M}_n = 0$ . Otherwise,  $\mathcal{M}_n = 1$ . Suppose the light curve under consideration is regularly observed (e.g.

with a space-based telescope such as Kepler) with missing-observations, then we shall define

$$\mathbf{F} = e^{\mathbf{A}\delta t}, \quad (54)$$

and

$$\mathbf{Q} = \int_0^{\delta t} e^{\mathbf{A}\xi} \mathbf{B} \mathbf{B}^\top e^{\mathbf{A}^\top \xi} d\xi, \quad (55)$$

where  $\mathbf{F}$  is called the transition matrix and  $\mathbf{Q}$  is the disturbance variance-covariance matrix. Then we may write the integrated state-equation (51) as

$$\mathbf{x}_{k+1} = \mathbf{F}\mathbf{x}_k + \mathbf{w}_k, \quad (56)$$

where  $\mathbf{w}_k \sim \mathcal{N}(\mathbf{0}, \mathbf{Q})$ . The original observation equation (48) remains unchanged through this process but is now discrete

$$\chi_n = \mathbf{H}_n \mathbf{x}_n + v_n, \quad (57)$$

where  $v_n \sim \mathcal{N}(0, \sigma_{N,n}^2)$  are (heteroskedastic) measurement errors. We recognize equations (56) and (57) as a discrete-time state-space system and identify it with the *Auto-Regressive Moving Average* (ARMA) processes of Brockwell & Davis (2009), Brockwell & Davis (2010), Durbin & Koopman (2012), and in astronomical variability studies of Scargle (1981); Gaskell & Peterson (1987); Koratkar & Gaskell (1991). If the light curve has missing observations, we recommend that the 1<sup>st</sup> canonical form from equation (49) be chosen. The benefit of this form of the state-space equations is that the observation matrix is very simple. To correctly handle missing-observations, it suffices to set  $\mathbf{H}_n = (\mathcal{M}_n \ 0 \ \dots \ 0 \ 0)$  and the measurement uncertainty of the  $n^{\text{th}}$  observation  $\sigma_{N,n}^2 = \infty$  (Jones 1993).

If the light curve is obtained with an IRS pattern as is usually the case with ground-based astronomical observations such as those carried out by the Sloan Digital Sky Survey (SDSS), we define  $\delta t_n = t_{n+1} - t_n$ . If the IRS pattern is fairly dense, it may be advantageous to simply determine an artificial fixed sampling interval  $\delta t$  as the greatest common divisor of the individual  $\delta t_n$ . Then we add missing-observations into the light curve so that the missing-observations correspond to the gaps in the original light curve. At this point, we may treat the formerly IRS light curve as a RS light curve with lots of missing observations.

If the IRS pattern is fairly sparse, it is computationally cheaper to recompute the transition matrix  $\mathbf{F}_n$  and the disturbance variance-covariance matrix  $\mathbf{Q}_n$  at every time step with

$$\mathbf{F}_n = e^{\mathbf{A}\delta t_n}, \quad (58)$$

and

$$\mathbf{Q}_n = \int_0^{\delta t_n} e^{\mathbf{A}\xi} \mathbf{B} \mathbf{B}^\top e^{\mathbf{A}^\top \xi} d\xi, \quad (59)$$

as proposed by Jones (1993) and Kelly et al. (2014). The exact IRS pattern for which the two methods are equally fast depends on the machine architecture and hence implementations of the C-ARMA modeling software should include both methods as options.

## 8 KALMAN FILTER ESTIMATION OF C-ARMA PROCESS PARAMETERS

Having obtained the discrete-time state- and observation-equations for the original C-ARMA process, we may now use the Kalman filter to compute the likelihood of having observed the light curve given the C-ARMA model. As stated earlier, one of the many attractive properties of the Kalman filter is that it operates sequentially on the light curve measurements—the Kalman filter uses the state-equation to predict the current state of the system based on the previous state before the observation is made available to the algorithm i.e. it computes an estimate of the *a priori* state of the system  $\hat{x}_n^-$ , where the ‘ $-$ ’ signifies that it is an *a priori* estimate. Once the  $n^{\text{th}}$ -observation is made available to the algorithm, the Kalman filter uses the observation to correct the *a priori* state of the system and thereby estimates the *a posteriori* state of the system  $\hat{x}_n^+$ , where the ‘ $+$ ’ signifies that it is an *a posteriori* estimate. We can use the estimated *a priori* states of the system  $\hat{x}_n^-$  to predict estimates of the observed flux  $\hat{y}_n = \mathbf{H}\hat{x}_n^-$ . The difference between the *a priori* predictions of the observed flux and the actual values of the observed flux,  $r_n$ , are known as ‘innovations’

$$r_n = y_n - \hat{y}_n, \quad (60)$$

and may be shown to be i.i.d. normal deviates (Simon 2006, chapter 10.2) that are distributed according to  $\mathcal{N}(0, S_n)$  where  $S_n$  is the estimate of the variance of the  $n^{\text{th}}$ -innovation.

Suppose we wish to calculate the log-likelihood of the C-ARMA( $p, q$ ) model  $C$  for the set of model parameters  $\alpha_k$  and  $\beta_k$  given the observed light curve of an object,  $\{y_n\}$ . From Bayes’ theorem,

$$\ln \mathcal{L}(C|\{y_n\}) = \ln \mathcal{L}(\{y_n\}|C) + \ln \mathcal{L}(C). \quad (61)$$

The log-likelihood of the observed light curve  $\{y_n\}$  given the model  $C$  may be computed using the innovations via

$$\ln \mathcal{L}(\{y_n\}|C) = \sum_{n=1}^N -\frac{\mathcal{M}_n}{2} (\ln 2\pi + \ln S_n + \frac{r_n^2}{S_n}), \quad (62)$$

where we include the value of the mask  $\mathcal{M}_n$  to ensure that missing-observations do not contribute to the log-likelihood. For the prior, i.e. the likelihood of the model itself, we use the piecewise function

$$\ln \mathcal{L}(C) = \begin{cases} 0 & \text{if } \operatorname{Re}(\rho_k) < 0 \text{ and } \operatorname{Re}(\mu_k) < 0 \text{ for all } k \\ -\infty & \text{otherwise} \end{cases}, \quad (63)$$

where  $\rho_k$  and  $\mu_k$  are the roots of the autoregressive and moving average polynomials. This prior, while uninformative for acceptable values of the roots, ensures that the C-ARMA process corresponding to the roots is both stable and invertible.

The innovations required for the calculation of the light curve likelihood in equation (62) may be computed by applying the Kalman filter to the observed flux measurements. To do so, we require an estimate of the initial state of the system  $\hat{x}_0^+$  as well as the uncertainty in the initial state of the system  $\mathbf{P}_0^+$ . The best estimate of the state of the system when initializing the Kalman filter is

$$\hat{x}_0^+ = 0 \quad (64)$$

and the state uncertainty may be computed by solving

$$(\mathbf{I} \otimes \mathbf{I} - \mathbf{F} \otimes \mathbf{F}) \operatorname{vec}(\mathbf{P}_0^+) = \operatorname{vec}(\mathbf{Q}), \quad (65)$$

for  $\mathbf{P}_0^+$  as shown in Durbin & Koopman (2012, chapter 5.6.2).

Then starting with the first observation, i.e.  $n = 1$ , we iterate through the  $N$  observations using the Kalman filter. We begin by computing the expected value of the *a priori* state:

$$\hat{x}_n^- = \mathbf{F}\hat{x}_{n-1}^+. \quad (66)$$

and the expected value of the *a priori* state uncertainty:

$$\mathbf{P}_n^- = \mathbf{F}\mathbf{P}_{n-1}^+\mathbf{F}^\top + \mathbf{Q}. \quad (67)$$

At this point, the innovation for this observation and the uncertainty in the innovation can be computed by comparing the expected observation to the actual observation using

$$r_n = y_n - \mathbf{H}\hat{x}_n^-, \quad (68)$$

and

$$S_n = (\mathbf{H}_n \mathbf{P}_n^- \mathbf{H}_n^\top + \sigma_{N,n}^2), \quad (69)$$

where  $\sigma_{N,n}^2$  is the (heteroskedastic) variance of the observation noise.

Before we may compute the innovation for the next observation, we must use our knowledge of the observed value of the AGN flux to update our knowledge of the state and the uncertainty in the state. Since the measurements are noisy, we must compute a gain to apply to the measurement. The gain should reflect the noisiness of the measurements i.e. if the  $n^{\text{th}}$ -observation is very noisy, we would like the gain that we apply to be very small. More significance is given to the observation as compared to the *a priori* state estimate if the gain is large. The optimal gain is the Kalman gain given by

$$\mathbf{K}_i = \mathbf{P}_i^- \mathbf{H}_i^\top S_i^{-1}. \quad (70)$$

While any gain value will yield an unbiased estimate of the state, the Kalman gain yields an unbiased *minimum variance* *a posteriori* estimate of the state and state uncertainty (Simon 2006, chapter 3.3). The Kalman gain is used to compute the *a posteriori* state and state covariance via

$$\hat{x}_i^+ = \hat{x}_i^- + \mathbf{K} r_i, \quad (71)$$

and

$$\mathbf{P}_i^+ = (\mathbf{I} - \mathbf{K}\mathbf{H}_i)\mathbf{P}_i^- (\mathbf{I} - \mathbf{K}\mathbf{H}_i)^\top + \mathbf{K}\sigma_i^2 \mathbf{K}^\top. \quad (72)$$

The innovations computed using this procedure may then be used along with equations (62) and (63) to compute the log-likelihood of the C-ARMA model  $C$  given the observed light curve  $\{y_n\}$  using equation (61). A multitude of numerical algorithms, including the Expectation-Maximization algorithm, can be used to maximize this likelihood. Alternatively, the full probability distribution of the C-ARMA model parameters can be probed by applying Markov Chain Monte Carlo (MCMC) techniques to the likelihood function.

## 9 MODEL SELECTION

Although we have reasons to expect AGN light curves to be well modelled by simple C-ARMA models of low order, it is prudent to search a large portion of the space of allowable

models and use a statistically sound information criteria to pick the optimal model order. Information criteria such as the corrected Akaike Information Criteria (AICc) and the Deviance Information Criteria (DIC) balance model likelihood against model simplicity. The model that minimizes a chosen information criteria is the most-likely maximally-parsimonious model that fits the observed light curve (Burnham & Anderson 2003).

If a non-linear optimization algorithm is used to maximize the likelihood in equation (61), we have point estimates of the model parameters and a single value for the likelihood of each model. To select the model order, we may use the AICc

$$AICc = 2(p + q + 1) - 2 \ln \mathcal{L}(C|yn) + \frac{2(p + q + 1)(p + q + 2)}{N - p - q - 2}, \quad (73)$$

where  $p$  and  $q$  are the orders of the C-ARMA( $p,q$ ) model and  $N$  is the number of observations in the light curve.

Markov Chain Monte Carlo (MCMC) can be used to sample the likelihood function of equation (61). Sampling the likelihood function yeilds reliable estimates of the confidence intervals of the C-ARMA model parameters even if the likelihood function is highly non-Gaussian. If multiple samples from the likelihood function are available, it is possible to use the DIC to select model order. THe DIC is given by

$$DIC = \mu_{D(C)} + \frac{1}{2} \sigma_{D(C)}^2, \quad (74)$$

where the deviance  $D(C)$  is computed as

$$D(C) = -2 \ln \mathcal{L}(C|yn). \quad (75)$$

Either one of the DIC or the AICc may be used to select the optimum model order.

We have shown that regardless of the form of the equation governing the flux emitted by AGN and without a detailed analytic prescription for the form of accretion disk instabilities, it is possible to model small stochastic fluctuations in the observed light curve of AGN as a C-ARMA process. The physics of the accretion process may be probed by examining the Green's function and the Disturbance PSD of the inferred C-ARMA process. We have presented a method for inferring the model parameters of the C-ARMA process from observations of the light curve using the Kalman filter that is particularly suitable for light curves with regular sampling. In the next section, we study the accretion physics of the Seyfert 1 AGN Zw 229-15 using data from the *Kepler* mission.



## 10 PROBING ACCRETION PHYSICS WITH THE *Kepler* SEYFERT 1 ZW 229-15

We apply the C-ARMA inferencing techniques decribed in sections 6 through 9 to the re-processed *Kepler* light curve of Zw 229-15 (*Kepler* catalog name KIC 006932990) using the software package CARMA\_PACK (Kelly et al. 2014). We begin by discussing data quality issues and the custom processing used to obtain the light curve that we analyze.

### 10.1 The *Kepler* Light Curve of Zw 229-15

The *Kepler* space mission was launched to quantify the frequency of Earth-sized and smaller planets around the habitable zone of nearby stars (Borucki et al. 2010). *Kepler* was designed to achieve this goal by using very-high precision photometry ( $\sim 20$  ppm of photometric noise) to monitor stellar sources in a  $115.6$  deg $^2$  FOV for planetary transits. The photometric precision requirement dictated that *Kepler* be launched as a 0.95 m Schmidt camera with an imager consisting of 42 CCDs of size  $50 \times 25$  mm with  $2200 \times 1024$  pixels each (image scale  $\sim 3.98$  arcsec per pixel) that are arranged in 21 modules with 4 readout channels each. Each integration consists of a 6.02 s exposure followed by a 0.502 s readout. The long-cadence light curves of interest for AGN variability studies are created by combining 270 integrations of duration 6.02 s each with 0.502 s readouts between each integration. The resulting in a sampling interval is  $\delta t = 29.43$  min (Van Cleve & Caldwell 2009; Christiansen et al. 2013).

Photometric accuracy requires that no pixel is allowed to oversaturate (Gilliland 2004). This goal is ensured by designing and operating the instrument under conditions such that the the *Kepler* PSF is large; a pixel-aperture of diameter 6.4 pixel is required to capture 95 percent of the encircled energy of a point-source. The large PSF is a source of crowding. Simple aperture photometry with the *Kepler* Science Operations Center (SOC) pipeline-defined aperture results in significant contamination from nearby sources. This is particularly problematic for extended sources such as Zw 229-15. Compounding the accuracy-issues are thermally-driven focus variations, pointing offsets, and differential velocity aberration. Some of the readout channels on certain CCDs have performance issues such as out-of-spec read noise levels and gain. Moire and rolling band effects are present in some channels (Kolodziejczak et al. 2010). Most of these issues are tracked in the form of co-trending basis vectors that quantify effects common to multiple targets across the FOV and can be used to detrend light curves of spacecraft-induced variability (Stumpe et al. 2012; Smith et al. 2012). However, the de-trended light curve of Zw 229-15 available on the Mikulski Archive for Space Telescopes (MAST) database is not consistent with ground-based observations (Kasliwal et al. 2015a).

To avoid the potential drawbacks of using the MAST-supplied SAP or PDCSAP light curve, we choose to use the Zw229-15 light curve of Williams & Carini (2015) and Carini & Ryle (2012). This re-processed light curve has been constructed to match ground-based observations. The *Kepler* SOC pipeline automatically determines the pixel-aperture for targets based on the target luminosity. While such automatically-determined apertures are adequate for observing planetary transits, they may capture too much flux from surrounding faint field-objects. The source flux can be re-extracted from customized pixel-aperture using the Python tool KEPEXTRACT supplied as part of the IRAF package PYKE (Kinemuchi et al. 2012). Ground-based observations of the luminosity of Zw 229-15, obtained as part of the reverberation mapping campaign of Barth et al. (2011), suggest that the ideal photometric aperture for Zw 229-15 is 50.24 arcsec $^2$ . Subsequent to the end of the reverberation mapping campaign, additional photometry was obtained by the Western Kentucky University group using the

1.3 m Robotically Controlled Telescope (Gelderman et al. 2003). Observations were obtained through a Johnson V filter using a cryogenically cooled CCD camera system with a SiTE CCD. Magnitudes were determined using differential photometry techniques employing the comparison sequence found in Barth et al. (2011). Host galaxy contamination was minimized by re-extracting the AGN flux from a 2-pixel aperture ( $31.6 \text{ arcsec}^2$ ) over the full duration the *Kepler* Zw 229-15 light curve. This aperture was found to minimize the difference between the *Kepler* light curve and the ground based observations while simultaneously removing the need to perform the ‘stitching’ required in the case of MAST-supplied light curve (Mushotzky et al. 2011; Edelson et al. 2013; Wehrle et al. 2013; Revalski et al. 2014; Kasliwal et al. 2015b).

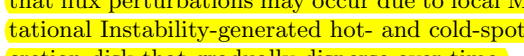
## 10.2 C-ARMA Analysis of the Zw 229-15 Light Curve

We used the C++ and Python library CARMA\_PACK of Kelly et al. (2014) to fit the observed light curve of Zw 229-15 to C-ARMA( $p,q$ ) processes with  $1 \leq p \leq 10$  and  $0 \leq q < p$ . Prior to the fitting, the light curve of Zw 229-15 was corrected to the rest-frame of the galaxy at  $z = 0.0275$  by scaling  $\delta t$  by  $1/(1+z)$ . No binning of the light curve was performed. Instead of adopting the *Kepler* error estimates, CARMA\_PACK assumes that the variance of the observation noise may be inaccurate and sets  $\sigma_{N,\text{true}}^2 = M_{\text{Err}}\sigma_{N,\text{stated}}^2$  for each observation. The multiplicative scaling factor  $M_{\text{Err}}$  is treated as a fit parameter i.e. all purely white noise in the data is assumed to originate in process of observation rather than be intrinsic to the signal. We find that the median value of the multiplicative scaling factor is  $M_{\text{Err}} = 1.30$ . The observation noise levels inferred from the pixel noise statistics of the *Kepler* CCDs appear to underestimate the true observation noise level in the signal by  $\sim 14$  percent (orange dash-dot line) at the 95-percent confidence level (dashed orange lines).

We searched an extensive space of C-ARMA models ( $1 \leq p \leq 10$  and  $0 \leq q < p$ ). The relatively simple C-ARMA(2,2) model achieved the lowest AICc value. The  value of  $-2333427.16925$  for the C-ARMA(2,1) model vs the value  $-2333328.70173$  for the C-ARMA(3,2) model (the next best model) suggests that the C-ARMA(3,2) is very unlikely ( $\sim 10^{-22}$  times as likely) to explain the observed data (Burnham & Anderson 2003). Figure 1 shows the full light curve of Zw 229-15 (orange) along with a  smoothed realization (grey). In addition to the expectation value of the smoothed realization, we show (light grey) the  $1\sigma$  limits on the smoothed light curve. Notice how this  $1\sigma$  limit is usually too small to be visible but increases dramatically when the observed light curve has missing values.  We also show a mock realization (green) of a light curve with C-ARMA(2,1) drawn randomly from the distribution of the parameters of the process describing the light curve of Zw 229-15. Figure 2 shows the median estimated PSD of the light curves of Zw 229-15 (grey) along with the 95<sup>th</sup>-percentile confidence region (light grey). From the reported *Kepler* noise estimates and the estimates of  $M_{\text{Err}}$ , we compute the noise level in the PSD using  $S_{NN} = 2\delta t M_{\text{Err}} \sigma_N^2$  where we use median values for  $M_{\text{Err}}$  and  $\sigma_N^2$ . We estimate the frequency  $\nu_{\text{noise}} \sim 2.9 \text{ d}^{-1}$  at which the PSD of the light

curve drops below the noise level by linearly interpolating the PSD between points. The corresponding timescale is  $t_{\text{noise}} \sim 8.3 \text{ h}$ . Since the PSD of the underlying flux variations drops below the PSD of the *Kepler* noise level at  $t_{\text{noise}}$ , we have no information about the behavior of the light curve on timescales shorter than  $\sim 8 \text{ h}$  and any features that appear on timescales of under  $\sim 16 \text{ h}$  should be regarded as dubious given the noise properties of *Kepler*. We mark the noise-dominated region of the PSD plot in the inset in red.

## 10.3 The Damped Harmonic Oscillator-like Behavior of the Light Curve

Since the Zw 229-15 light curve is well-described by a C-ARMA(2,1) process, the differential equation governing the behavior of flux perturbations may be interpreted as the damped harmonic oscillator driven by a colored stochastic process as described in section 5. Figure 3 shows the distribution of the undamped-oscillator time period  $T_{\text{dHO}}$  against the damping ratio  $\zeta_{\text{dHO}}$ . The damping ratio is very large with median value 3.30 with 95-percent CI [2.78,3.85] while the time period of the harmonic oscillator in the absense of damping is 59.9 d with 95-percent CI [56.9,62.8] d. Physically, this implies that perturbations of the flux do not oscillate about the mean-level but instead slowly return to the steady-stae flux level.  This observation supports the idea that flux perturbations may occur due to local Magneto Rotational Instability-generated hot- and cold-spots in the accretion disk that gradually disperse over time.

The corresponding Green’s function is shown in figure 4 along with the 95 percent CI. Recall that the Green’s function quantifies the evolution of a ‘unit-impusle’. In this case, the impulses consist of perturbations of the flux away from the steady-stae level. The effect of an impulse is to drive the flux away from the mean-level until the rate at which the flux is changing drops to zero. This occurs  $t_{\text{max}} = 5.65 \text{ d}$  with 95-percent CI [5.50,5.80] d after the original impulse (orange dashed line). On the left hand side of the figure, we see that on short timescales (red-shaded region) the observation noise makes it impossible to observe structure in the Green’s function. However, the  $t_{\text{max}} \sim 5.6 \text{ d}$  timescale that we detect here is safely above  $t_{\text{noise}} \sim 8.3 \text{ h}$  and is therefore unlikely to be an artifact of the instrumentation-noise. Due to the very large damping ratio, flux perturbations do not dissipate rapidly—perturbations drop in intensity from the peak by a factor of e by  $t_{\text{e-fold}} = 68.7 \text{ d}$  with 95-percent CI [62.38,75.08] d. On longer timescales, the correlation between the total integrated flux from the accretion disk and the original perturbation will decrease as the flux becomes dominated by the increasingly larger numbers of intervening perturbations. It is plausible that conventional approaches such as PSD-fitting and structure function analysis detect the  $t_{\text{e-fold}}$  timescale as the de-correlation timescale.

Figure 5 shows the PSD of the disturbance properties inferred from the estimates of  $\beta_1$  and  $\beta_2$  i.e. the powerspectrum of the impulses that drive the flux perturbations. On very long timescales, the disturbance have equal power over  $\sim 3.5$  decades of frequency. On timescales of  $\sim 1 \text{ d}$ , the disturbance PSD begins to rise with log-slope 2. Impulses with such PSD resemble ‘violet noise’. Such PSD are produced by the thermal noise of the medium (Mellen 1952) suggesting that on these very short timescales, we may be probing

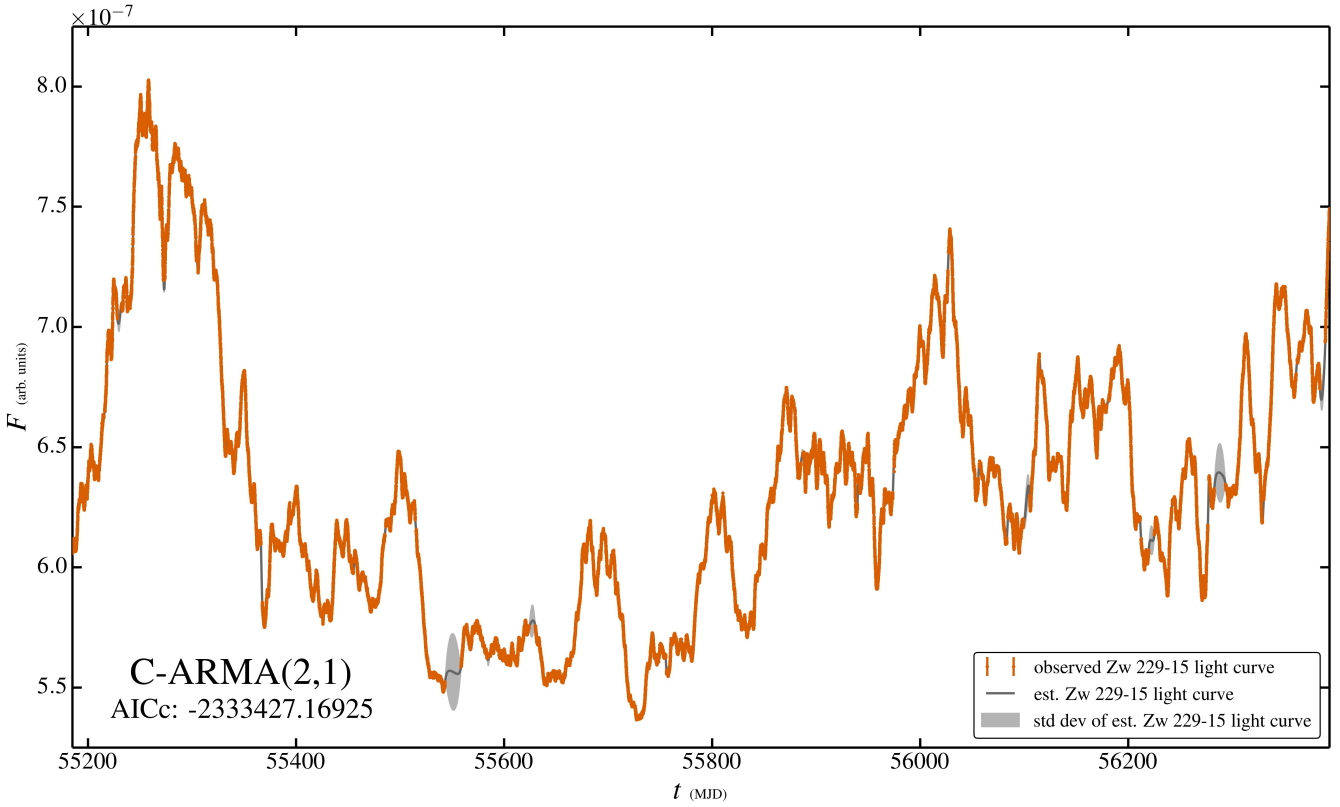


**Figure 1.** Light curve of the Seyfert 1 AGN Zw 229-15. This light curve is best fit by the C-ARMA(2,1) process discussed in section 5.

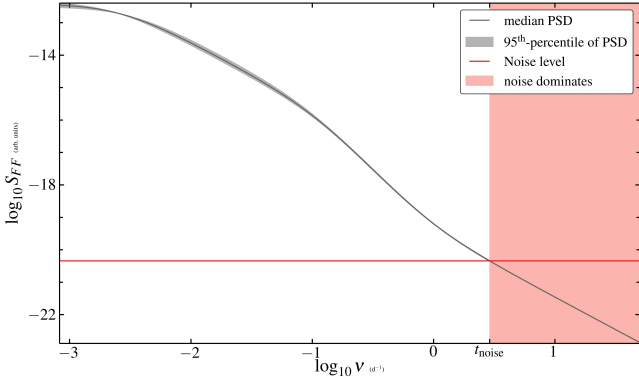


**Figure 2.** Power spectral density of the light curve of Zw 229-15. Using the *Kepler* noise properties  $\sigma_{N,\text{stated}}^2$  and  $M_{\text{Err}}$ , we compute the observation noise level (red line). The inferred PSD crosses the noise level at  $t_{noise} \sim 8.3$  h. On timescales comparable to  $t_{noise}$ , i.e.  $< 1$  d, the noise level does not permit us to infer anything about the behavior of this light curve.

the accretion disk matter directly. Unfortunately, the proximity of the inferred turnover timescale  $t_{\text{turn}} = 1.081$  d with 95-percent CI [1.05, 1.11] d to the noise-dominated timescale  $t_{noise} \sim 8.3$  h makes it impossible to draw conclusions about the disturbance PSD behavior on these timescales.

Figure 6 shows that the estimates of  $t_{\text{max}}$  and of  $t_{\text{e-fold}}$  are anti-correlated with correlation coefficient  $-0.7$  while the estimates of  $t_{\text{max}}$  and of  $t_{\text{turn}}$  are correlated with correlation

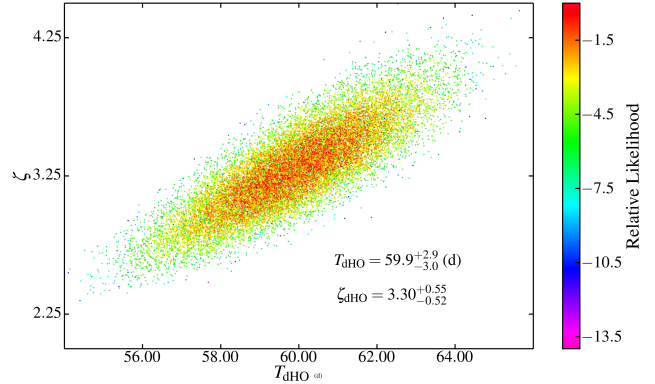


**Figure 3.** Damped Harmonic oscillator parametrization of the light curve of Zw 229-15.  $T$  is the time period of the undamped oscillator and  $\zeta$  is the damping ratio. Since  $\zeta > 1$ , the system is over-damped—flux perturbations in the accretion disk of Zw 229-15 decay to the steady-state flux level without oscillating.

coefficient 0.7. Estimates of  $t_{\text{e-fold}}$  have an order of magnitude larger spread than the estimates of  $t_{\text{max}}$ . Future variability studies, such as with the LSST, that probe a much longer temporal baseline, should help constrain the value of  $t_{\text{e-fold}}$  more tightly.

If the C-ARMA model is not estimated correctly, mock light curves generated using the model will not resemble the observed light curve. To visually test the C-ARMA(2,1)

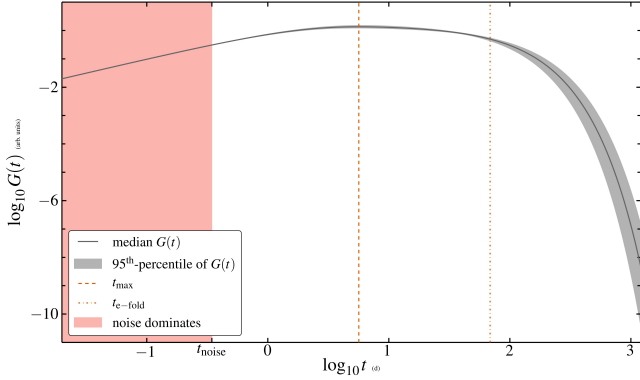


**Figure 4.** The Green’s function for the light curve of Zw 229-15 quantifies how a unit impulse flux perturbation evolves as a function of time. A tiny unit impulse perturbation at  $t = 0$  causes the flux from the perturbation to peak at  $t = t_{\max}$  ( $\sim 5.65$  d). The flux perturbation then decays, dropping to under  $\sim 1$  percent the peak intensity  $\sim 320$  d later. ~~The inset show the distribution of the roots of the autoregressive polynomial used to compute the Green’s function.~~

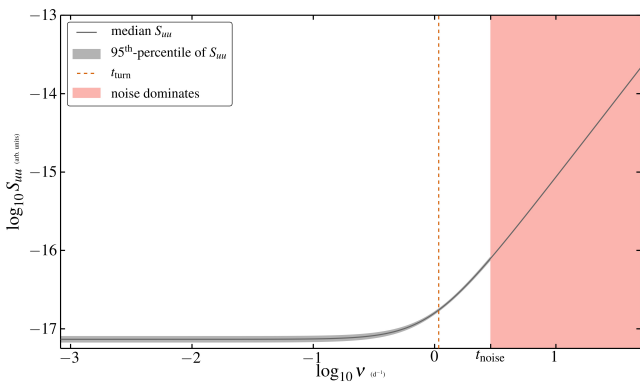


**Figure 5.** PSD of the flux perturbation impulses in the accretion disk of Zw 229-15. The PSD begins to steepen at  $t = t_{\text{turn}}$  ( $\sim 1$ ) d i.e. on timescales longer than  $\sim 1$  d, the flux perturbation impulses behave like white noise. On shorter timescales, the PSD approaches that of violet noise.

model inferred by us, we randomly selected sets of model parameter values, i.e. sets of values of  $\alpha_1$ ,  $\alpha_2$ ,  $\beta_1$ , and  $\beta_2$ , and generated simulated light curves using these parameters with the same sampling and noise levels as the true light curve. Figure 7 shows a sample of three such mock light curves along with the true light curve (orange). Visually all four light curves look very similar suggesting that the C-ARMA(2,1) is capturing most of the information in the light curve.

The light curve of Zw 229-15 observed by *Kepler* is well-described by a C-ARMA(2,1) process suggesting that a 2<sup>nd</sup>-order (probably non-linear) differential equation may be responsible for smoothing out flux perturbations over time. The *Kepler* data suggest that the impulses to the flux that drive the perturbations have equal power on timescales ranging from days to years. Perturbations to the flux behave like over-damped harmonic oscillators—the perturbation peaks in

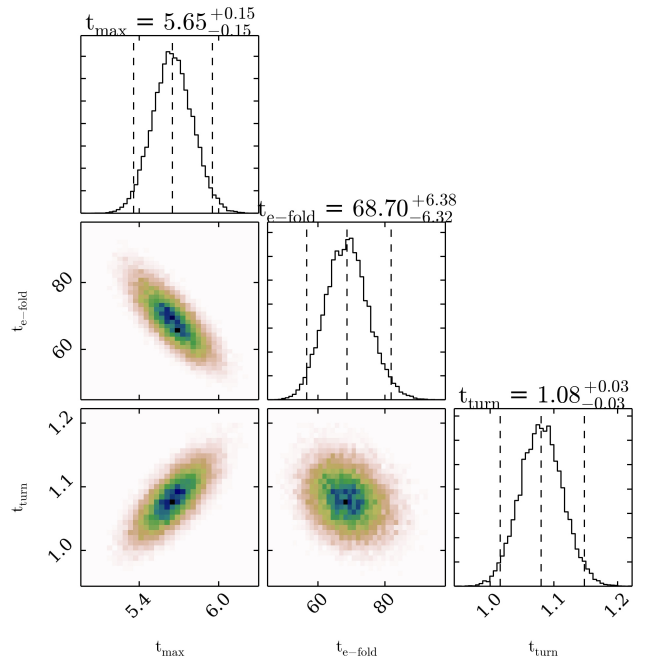


**Figure 6.** Scatter plots of  $t_{\max}$  v/s  $t_{e\text{-fold}}$  v/s  $t_{\text{turn}}$ . The diagonal shows histograms of the estimates of these timescales. The time taken to achieve peak output flux,  $t_{\max}$  is anti-correlated with the e-folding time of the flux perturbation  $t_{e\text{-fold}}$  but correlated with  $t_{\text{turn}}$ .

intensity at  $\sim 5.6$  d after which it gradually decays in intensity with an e-folding timescale of  $\sim 69$  d. On very short timescales ( $\sim 1$  d) there are indications that the impulse powerspectrum begins to rise with log-PSD slope 2 which may be due to the thermal motion of the accretion disk plasma. However, the observation noise level makes it difficult to probe accretion physics on these timescales. We discuss the effect of the *Kepler* noise characteristics on our results in the next section.

#### 10.4 Moire Pattern Noise

Instrument-induced artifacts were expected in the *Kepler* data prior to launch based on extensive ground-testing (Kolodziejczak et al. 2010). Further testing was performed during the commissioning of the telescope. Based on the testing, it was determined that several artifacts did not require mitigation for the primary science mission of *Kepler* i.e. exo-planet detection. Kolodziejczak et al. (2010) recommended strategies for correcting or flagging several of the artifacts generated by the *Kepler* detector electronics. Some of these recommendations have been implemented in the new *Dynablock* module (Clarke et al. 2014) that has been added to the *Kepler* SOC pipeline for Data Release 24 (Thompson et al. 2015). The light curve that we analyze here is *not* created using the per-pixel data provided by DR24—therefore we perform a test to quantify the effects of the various *Kepler* detector-induced artifacts on the results presented in section 10.3.

The *Kepler* focal plane science CCDs are read out over 84 channels that are referred to using the module# .output#

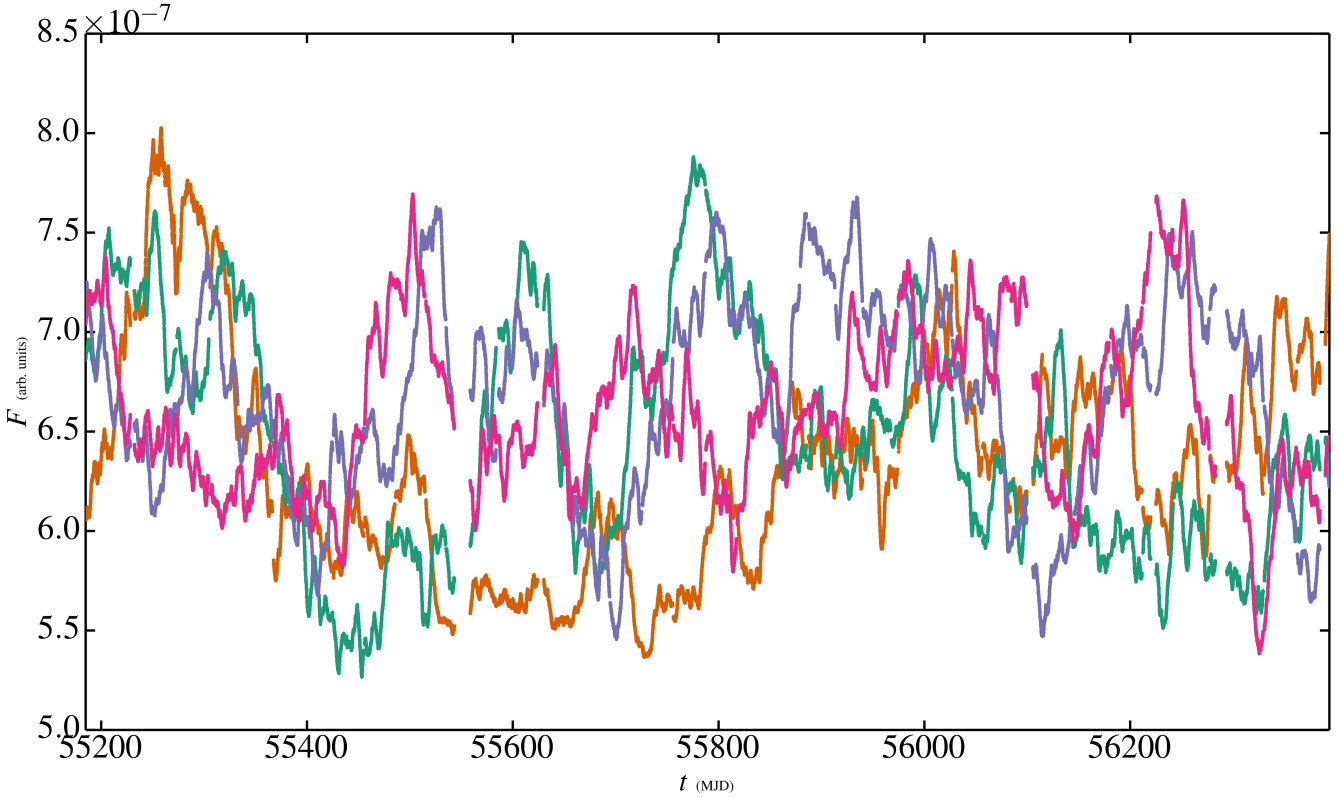


**Figure 7.** Simulated light curves with parameters drawn from the MCMC estimates of the C-ARMA(2,1) parameters of Zw 229-15. The true light curve of Zw 229-15 is also plotted. Can the true light curve be distinguished by eye?

convention presented in [Van Cleve & Caldwell \(2009\)](#) and in [Kasliwal et al. \(2015b\)](#). Zw 229-15 lands on the module#.output# combinations 14.48, 8.24, 12.40, and 18.64 as the *Kepler* focal plane performs a 90 degree rotation after every quarter i.e. the first quarter of Zw 229-15 data, obtained during quarter 4 (Q4) of the *Kepler* mission were read out over 14.48. Zw 229-15 landed on 14.48 again during quarters Q8, Q12, and Q16. Of these module#.output# combinations, 14.48 exhibits moderate levels of rolling band and moire artifacts while 12.40 has an out of specification undershoot—see [Van Cleve & Caldwell \(2009\)](#) for a detailed explanation of the sources of these artifacts. We assess the impact of the rolling-band and moire artifacts by removing the affected quarters (Q4, Q8, Q12, and Q16) from the light curve and re-doing the C-ARMA model fit.

We find that the C-ARMA(2,1) model still provides the best AICc value i.e. the order of the fit was not sensitive to the moire and rolling band issues. The inferred excess instrumentation noise is  $M_{\text{Err}} \sim 1.24$  which implies that the measurement errors are  $\sim 11.3$  percent higher than the quoted value. This suggests that there is an systematic underestimation of the *Kepler* observation noise level that cannot be attributed to the abnormal channel. From the inferred observation noise level, we find that the noise confusion limit drops slightly to  $t_{\text{noise}} = 7.9$  h. The largest change is manifest in the value of the damping ratio of the damped harmonic oscillator  $\zeta_{\text{dHO}} = 2.97$  with 95-percent CI [2.40, 3.57] while the time period of the harmonic oscillator remains  $T_{\text{dHO}} = 59.0$  d with 95-percent CI [55.4, 62.6] d. The Green's function peaks

$t_{\text{max}} = 5.89$  d after the initial perturbing impulse with 95-percent CI [5.54, 6.26] d, after which it begins to slowly decay with an e-folding time of  $t_{\text{e-fold}} = 61.7$  d with 95-percent CI [48.8, 76.0] d. The turnover timescale on which the driving impulse PSD is observed to begin rising with log-PSD slope 2 occurs at  $t_{\text{turn}} = 1.16$  d with 95-percent CI [1.08, 1.24] d.

All of these estimates are consistent (to within the 95-percent confidence intervals computed) with the corresponding values for the full light curve. This suggests that while the data obtained over module and output 14.48 have higher levels of observation noise and spacecraft-induced systematics, the observed behavior of Zw 229-15 cannot be attributed to observational issues and has physical significance.

## 10.5 Discussion

The optical variability properties Zw 229-15 has been extensively studied by multiple groups with various analysis techniques. [Mushotzky et al. \(2011\)](#) discovered the inconsistency of light curve of Zw 229-15 with the damped random walk (DRW) of [Kelly et al. \(2009\)](#) by analyzing the PSD of the first 4 quarters of the light curve. They reported values for the short timescale log-PSD slope between  $-2.96$  (Q8) and  $-3.31$  (Q6) by fitting the estimates of the PSD directly. Similarly high values were reported by [Carini & Ryle \(2012\)](#) who fit two PSD models to quarters 4 through 7 of the re-processing of light curve analyzed here and found log-PSD slopes  $-2.88$  and  $-2.83$  for a knee and broken power-law model respectively.

The full *Kepler* light curve of Zw 229-15 was analyzed using PSD and C-ARMA analysis methods by Edelson et al. (2014). Unlike the re-processing of Williams & Carini (2015) used by us and in Kasliwal et al. (2015a), Edelson et al. (2014) use a much larger pixel-aperture (32-pixels) to minimize spacecraft-induced variability due to thermally-induced focus variations and differential velocity aberration-known issues with *Kepler* light curves (Kinemuchi et al. 2012). At the same time, using such large masks results in crowding problems—faint background sources bleed flux into the aperture because of the large *Kepler* PSF contaminating the light curve with thier variability. The simple PSD analysis of the re-processed light curve suggests that on timescales longer than  $\sim 5.6$  d, the PSD is well modelled by a power law with log-slope  $-2$ . On shorter timesclaes, the log-PSD slope is much higher ( $-4.51$ ). There is an extra PSD component with log-PSD slope  $-1.28$  that contributes mostly at the 1 d timescale. The C-ARMA analysis uses the same software package (CARMA\_PACK) used by us and found a bend timescale of  $\sim 4$  d with log-PSD slopes  $-1.99$  and  $-3.65$  on longer and shorter timescales. Edelson et al. (2014) tested the light curve for moire pattern noise and found evidence to suggest that moire pattern noise is a significant contaminant in both the flagged and un-flagged quarters.

Kasliwal et al. (2015b) analyzed several *Kepler* MAST light curves that had been de-trended of spacecraft-induced varaibility by the *Kepler* SOC pipeline using co-trending basis vectors to quantify light curve features common to targets across teh *Kepler* FOV. Using a structure function method to fit a bent power-law PSD model, Kasliwal et al. (2015b) find log-PSD slope  $-2.7$  with characteristic de-correlation timescale  $27.5$  d.

Most recently, Williams & Carini (2015) applied a PSD analysis to the full light curve studied here and found log-PSD slope  $2.80 \pm 0.43$  with turnover timescale  $66.94^{+14.3}_{-11.8}$  d. The same log-PSD slope was found by Kasliwal et al. (2015a) using the structure function approach of Kasliwal et al. (2015b) suggesting that the slope and timescale found by Williams & Carini (2015) is significant and not sensitive to the analysis technique.

Regardless of the mechanism for variability, certain timescales of interest may be associated with a thin disk. The shortest timescale the light crossing timescale

$$t_{lc} \sim \frac{r_{lc}}{c} \quad (76)$$

where  $r_{lc}$  is the maximum radius that can be ascribed to  $t_{lc}$  (Peterson 1997) i.e. this timescale places a (very conservative) upper limit on the size of the region that variations could originate from. The shortest timescale on which variations should occur is the dynamical timescale given by

$$t_{dyn} \sim \frac{r}{v_{Kep}} = \left( \frac{r^3}{GM_{BH}} \right)^{\frac{1}{2}}, \quad (77)$$

where  $v_{Kep}$  is the Keplerian rotation velocity. Perturbations to hydrostatic equilibrium in the vertical ( $z$ ) direction are smoothed out on timescale

$$t_z \sim \frac{H}{c_S} \sim t_{dyn}, \quad (78)$$

which may be observable in the form of quasi-periodic variations in the light curve. Deviations from thermal equilibrium, caused by fluctuations in the local dissipation rate, are

damped out on the timescale

$$t_{therm} \sim \frac{c_S^2 r^2}{v_{Kep}^2 \nu} \sim \frac{t_{dyn}}{\alpha}. \quad (79)$$

Under the effect of viscous torques, matter diffuses through the disc on the viscous timescale,

$$t_{visc} \sim \frac{r^2}{\nu} \sim \frac{t_{dyn}}{\alpha(H/r)^2}. \quad (80)$$

The Barth et al. (2011) reverberation mapping study of Zw 229-15 suggest that  $M_{BH} = 1.0^{+0.19}_{-0.24} \times 10^7 M_\odot$  with  $r_{Sch} = 2GM/c^2 \sim 3 \times 10^{10}$  m or  $0.2$  au. The bolometric luminosity was found to be  $L_{bol} = 6.4 \times 10^{43}$  erg s $^{-1}$  corresponding to  $L/L_{Edd} \sim 0.05$ . Assuming disk radii of  $100r_{Sch}$  (20 au) to  $10000r_{Sch}$  (2000 au), Shakura Sunyaev  $\alpha$  parameter value between  $0.1$  and  $0.5$ , and disc height to radius ratios between  $0.01$  and  $0.1$ , we can compute the various timescales of equations (76) through (80).

The smallest viscous timescale is just under 1 yr suggesting that viscous fluctuations generated by the  $\alpha$  parameter variations of Lyubarskii (1997) are unlikely to be responsible for the observed variability.  $\alpha$  parameter variations in the Lyubarskii (1997) theory result in inward propogating fluctuations characterized by correlations between variability in different bands with hard lags i.e. shorter wavelength bands lag longer wavelength bands. This phenomenon is typically observed only in the X-rays (Vaughan & Fabian 2004; McHardy et al. 2004; Arévalo et al. 2006), whereas in the UVOIR the situation is reversed with longer wavelength bands lagging shorter wavelength bands (Wanders et al. 1997; Sergeev et al. 2005).

Estimates of the thermal timescales can range between  $sim3$  d ( $r = 10^2 r_{Sch}$  &  $\alpha = 0.5$ ) and  $sim5$  yr ( $r = 10^4 r_{Sch}$  &  $\alpha = 0.1$ ) making it plausible to associate the  $t_{e-fold} = 69$  d timescale with the thermal timescale of the disc. This may imply that the variability observed by *Kepler* in the optical is driven by the unobserved X-ray variability of Zw 229-15 (Krolik et al. 1991). However, it is now known that while X-ray variability drives small scale fluctuations in optical variability on short timescales, longer timescale large amplitude fluctuations exist in the optical that are too energetic to be driven by re-processed X-ray emission (Uttley et al. 2003; Arévalo 2009). There is strong evidence to suggest that there are *two* sources of variability in the optical–reprocessing of X-ray emissions that drives short timescale low-amplitude variability, and a process local to the optical emitting region of the disk that drives larger amplitude, longer timescale changes (Gaskell 2008). While the *Kepler* light curve of Zw 229-15 is long enough to probe the days–weeks timescales associated with the re-processing of the X-ray variability, it may not be sensitive to the longer timescale variability intrinsic to the optical.

The dynamical timescale of the disk ranges between  $\sim 1.6$  and  $\sim 1600$  d making it plausible to associate the observed  $t_{e-fold}$  with this quantity as well. The dynamical timescale characterizes states that are perturbed from dynamical equilibrium such as by global g-modes (Reynolds & Miller 2009; O’Neill et al. 2009). The light crossing timescale is smaller than  $\sim 11$  d making it unsuitable to associate with any of the timescales that we have measured.

We have sucessful recovered the  $\sim 5.6$  d timescale found

by [Edelson et al. \(2014\)](#). We interpret it as the time lag at which the Green's function peaks i.e. the duration between the initial impulse driving a flux perturbation and the peak in emitted flux. We have found that there is some indication of excess power at very high frequencies ( $> 1 \text{ d}^{-1}$ ) though the observation noise level makes the detection dubious. We treat this excess power as belonging purely to the disturbance process that generates the stochastic variability—in which case it may be caused by the thermal noise of emitting medium. We identify the 67 d timescale reported by [Williams & Carini \(2015\)](#) with the e-folding timescale  $t_{\text{e-fold}}$  of a flux perturbation in the accretion disk of the AGN i.e. it is the duration over which flux perturbations decay by a factor of e. Finally, we point out that the exact slope of the log-PSD is purely a function of frequency. From the C-ARMA(2,1) PSD in equation (40), we see that over a considerable range of frequencies, one may expect the log-PSD to have slope close to  $-2$ . At very high frequencies, the log-PSD approaches  $-4$  as the  $\nu^4$  term in the denominator of equation (40) begins to dominate. At very low frequencies, we expect the PSD to flatten. This is exactly the behavior inferred by all the studies of Zw 229-15 and is predicted of the C-ARMA(2,1) process. The reason why different studies have fit a range of slopes at different frequencies is attributable to variations between the exact processing used and sensitivity to different parts of the PSD.

## 11 CONCLUSIONS

We have developed a powerful tool to probe AGN accretion physics using variability. Small perturbations of the total flux emitted by an AGN can be modelled in the linear-regime as a linear differential equation driven by noise, or a Continuous-time AutoRegressive Moving Average (C-ARMA) process. Such processes consist of an  $n^{\text{th}}$ -order linear differential equation for the flux perturbation on the LHS and a linear combination of Wiener increments and derivatives on the RHS. The Wiener increments are viewed as stochastically driving the flux perturbations and characterize complex MHD processes. Insights into the variability-driving physics can be obtained by examining the PSD of the driving disturbances to the accretion disk flux. The linear differential equation on the LHS of the C-ARMA process governs how flux perturbations evolve after they have been generated. The evolution of the flux perturbations can be characterized by the Green's function of the linear-differential equation.

In the case of a simple noise-driven damped harmonic oscillator or C-ARMA(2,1) process, the Green's function increases steeply over a characteristic timescale  $t_{\text{max}}$  before decaying exponentially with a e-folding timescale  $t_{\text{e-fold}}$ . The driving disturbances have a flat PSD on long timescales that increases as  $\nu^2$  on timescales shorter than  $t_{\text{turn}}$ . The short timescale behavior of the PSD may arise from the thermal motion of the material in the accretion disk.

We present two representations of the C-ARMA process in state-space form. The first representation puts the dynamics of the flux variations into the state-equation and possesses a very simple form for the observation equation. We argue that this representation is ideally suited for analyzing well-sampled flux light curves with constant sampling rate even in

the presence of missing observations. The second representation, used by [Kelly et al. \(2014\)](#), spreads the dynamics of the flux variations across the state- and observation-equations. We present a simple form of the Kalman filtering equations and demonstrate how they can be applied to infer the values of the co-efficients in the linearized flux perturbation equation.

We have analyzed a custom re-processing of the optical light curve of the Seyfert 1 galaxy Zw 229-15 using the C-ARMA formalism. This re-processed light curve is consistent with ground-based observations of Zw 229-15 ([Williams & Carini 2015](#)). We find that the optical flux variations in Zw 229-15 can be viewed as arising from a damped harmonic oscillator driven by colored noise i.e. the C-ARMA(2,1) model of section 5. The light curve fluctuations are strongly damped with damping ratio  $\zeta = 3.3$ . Hence perturbations to the flux result in a smooth decay to the steady-state flux level with no oscillatory behavior. The Green's function of the flux perturbations is observed to peak on timescale  $t_{\text{max}} = 5.6 \text{ d}$  which is consistent with the PSD timescale reported by [Edelson et al. \(2014\)](#). After the initial peak, flux perturbations decay with e-folding timescale  $t_{\text{e-fold}} = 69 \text{ d}$  which is consistent with the PSD timescale reported by [Williams & Carini \(2015\)](#). We find that on timescales shorter than  $\sim 1 \text{ d}$ , the PSD of the disturbances rises steeply as  $\nu^2$ , however the measurement noise level of *Kepler* makes this finding tentative. We hunt for non-physical spacecraft-induced contributions to the observed behavior by examining the effect of moire-pattern noise on our results. While the moire-pattern noise affected quarters have slightly higher measurement noise than the clean quarters, the overall model-fit does not change significantly when excluding the noisy quarters. We conclude that the variability behavior observed in Zw 229-15 by *Kepler* is well-characterized as arising from a very over-damped harmonic oscillator driven by a colored-noise process. Breaks and features found in PSD analysis of light curves may be interpreted in the context of characteristic timescales in the Green's function that governs how flux perturbations evolve and the PSD of driving colored noise process.



## ACKNOWLEDGEMENTS

We acknowledge support from NASA grant NNX14AL56G. This paper includes data collected by the Kepler mission. Funding for the Kepler mission is provided by the NASA Science Mission directorate. Some of the data presented in this paper were obtained from the Mikulski Archive for Space Telescopes (MAST). STScI is operated by the Association of Universities for Research in Astronomy, Inc., under NASA contract NAS5-26555. Support for MAST for non-HST data is provided by the NASA Office of Space Science via grant NNX09AF08G and by other grants and contracts.

## REFERENCES

- Abramowicz M. A., Czerny B., Lasota J. P., Szuszkiewicz E., 1988, *ApJ*, **332**, 646  
 Abramowicz M. A., Chen X., Kato S., Lasota J.-P., Regev O., 1995, *ApJ*, **438**, L37

- Arévalo P., 2009, in Wang W., Yang Z., Luo Z., Chen Z., eds, Astronomical Society of the Pacific Conference Series Vol. 408, The Starburst-AGN Connection. p. 296
- Arévalo P., Papadakis I. E., Uttley P., McHardy I. M., Brinkmann W., 2006, *MNRAS*, **372**, 401
- Balbus S. A., Hawley J. F., 1991, *ApJ*, **376**, 214
- Balbus S. A., Hawley J. F., 1992, *ApJ*, **400**, 610
- Balbus S. A., Hawley J. F., 1997, in Wickramasinghe D. T., Bicknell G. V., Ferrario L., eds, Astronomical Society of the Pacific Conference Series Vol. 121, IAU Colloq. 163: Accretion Phenomena and Related Outflows. p. 90
- Balbus S. A., Papaloizou J. C. B., 1999, *ApJ*, **521**, 650
- Barth A. J., et al., 2011, *ApJ*, **732**, 121
- Blaes O., 4, in Maurizio F., Belloni T., Casella P., Gilfanov M., Jonker P., King A., eds, Space Sciences Series of ISSI, Vol. 49, The Physics of Accretion onto Black Holes. Springer, Chapt. 2, pp 21–42
- Blandford R. D., Payne D. G., 1982, *MNRAS*, **199**, 883
- Borucki W. J., et al., 2010, *Science*, **327**, 977
- Brockwell Peter J., 1994, in Tong H., ed., Nonlinear Time Series and Chaos, Vol. 1, Dimension Estimation and Models. World Scientific Pub. Co. Inc., Chapt. 4, pp 170–190
- Brockwell Peter J., 2001, in Shanbhag D. N., Rao C. R., eds, Handbook of Statistics, Vol. 19, Stochastic Processes. North-Holland, Chapt. 9, pp 249–276
- Brockwell P., 2014, *Ann. Inst. Stat. Math.*, **66**, 647
- Brockwell Peter J., Davis Richard A., 2009, Time Series: Theory and Methods, 2 edn. Springer Texts in Statistics, Springer
- Brockwell Peter J., Davis Richard A., 2010, Introduction to Time Series and Forecasting, 2 edn. Springer Texts in Statistics, Springer
- Burnham K. P., Anderson D. R., 2003, Model Selection and Multimodel Inference: A Practical Information-Theoretic Approach, 3 edn. Springer
- Carini M. T., Ryle W. T., 2012, *ApJ*, **749**, 70
- Chen X., Abramowicz M. A., Lasota J.-P., Narayan R., Yi I., 1995, *ApJ*, **443**, L61
- Christiansen J. L., et al., 2013, Technical Report KSCI-19040-004, Kepler Data Characteristics Handbook. National Aeronautics and Space Administration, NASA Ames Research Center, Moffett Field, California
- Clarke B., Kolodziejczak J. J., Caldwell D. A., 2014, in American Astronomical Society Meeting Abstracts #224. p. 120.07
- Coriat M., Fender R. P., Dubus G., 2012, *MNRAS*, **424**, 1991
- Davis J. H., 2002, Foundations of Deterministic and Stochastic Control. Birkhäuser
- Denham M. J., 1974, *IEEE Transactions on Automatic Control*, **19**, 646
- Dexter J., Agol E., Fragile P. C., 2009, *ApJ*, **703**, L142
- Dexter J., Agol E., Fragile P. C., McKinney J. C., 2010, *ApJ*, **717**, 1092
- Dickinson B. W., Kailath T., Morf M., 1974, *IEEE Transactions on Automatic Control*, **19**, 656
- Done C., 2014, in Martínez-Paía I. G., Shahbaz T., Velázquez J. C., eds, Canary Islands Winter School of Astrophysics, Accretion Processes in Astrophysics. Cambridge University Press, Chapt. 6, pp 184–226
- Doob Joseph L., 1990, Stochastic Processes. Wiley-Interscience
- Durbin J., Koopman S. J., 2012, Time Series Analysis by State Space Methods, 2 edn. Oxford Statistical Science Vol. 38, Oxford University Press
- Edelson R. A., et al., 1996, *ApJ*, **470**, 364
- Edelson R., Mushotzky R., Vaughan S., Scargle J., Gandhi P., Malkan M., Baumgartner W., 2013, *ApJ*, **766**, 16
- Edelson R., Vaughan S., Malkan M., Kelly B. C., Smith K. L., Boyd P. T., Mushotzky R., 2014, *ApJ*, **795**, 2
- Emmanoulopoulos D., McHardy I. M., Uttley P., 2010, *MNRAS*, **404**, 931
- Fragile P. C., Blaes O. M., 2008, *ApJ*, **687**, 757
- Fragile P. C., Blaes O. M., Anninos P., Salmonson J. D., 2007, *ApJ*, **668**, 417
- Frank J., King A., Raine D., 2002, Accretion Power in Astrophysics, 3 edn. Cambridge University Press
- Friedland B., 2005, Control System Design: An Introduction to State-Space Methods. Dover Books on Electrical Engineering, Dover Publications
- Froning C. S., et al., 2011, *ApJ*, **743**, 26
- Gaskell C. M., 2008, in Revista Mexicana de Astronomía y Astrofísica Conference Series. pp 1–11 ([arXiv:0711.2113](https://arxiv.org/abs/0711.2113))
- Gaskell C. M., Peterson B. M., 1987, *ApJS*, **65**, 1
- Gelderblom R., Guinan E., Howell S., Mattox J. R., McGruder C. H., Walter D. K., Davis D. R., Everett M., 2003, in American Astronomical Society Meeting Abstracts #202. p. 766
- Gierliński M., Middleton M., Ward M., Done C., 2008, *Nature*, **455**, 369
- Gillespie D. T., 1996, *American Journal of Physics*, **64**, 225
- Gilliland R. L., 2004, Technical report, ACS CCD Gains, Full Well Depths, and Linearity up to and Beyond Saturation. Space Telescope Science Institute
- Grewal M. S., Andrews A. P., 2010, *IEEE Control Systems Magazine*, **30**, 69
- Grindlay J. E., Miller G. F., Siemiginowska A., Los E., Kelly B. C., Tang S., 2014, in American Astronomical Society Meeting Abstracts #224. p. 410.05
- Hameury J.-M., Viallet M., Lasota J.-P., 2009, *A&A*, **496**, 413
- Hamilton J. D., 1994, Time Series Analysis. Princeton University Press
- Harvey A. C., 1991, Forecasting, Structural Time Series Models and the Kalman Filter. Cambridge University Press
- Hawley J. F., Balbus S. A., 1991, *ApJ*, **376**, 223
- Hawley J. F., Balbus S. A., 1992, *ApJ*, **400**, 595
- Hawley J. F., Gammie C. F., Balbus S. A., 1995, *ApJ*, **440**, 742
- Henisey K. B., Blaes O. M., Fragile P. C., 2012, *ApJ*, **761**, 18
- Jacobs K., 2010, Stochastic Processes for Physicists: Understanding Noisy Systems. Cambridge University Press
- Janiuk A., Czerny B., 2007, *A&A*, **466**, 793
- Jones R. H., 1993, Longitudinal Data with Serial Correlation: A State-Space Approach. Monographs on Statistics and Applied Probability Vol. 47, Chapman & Hall
- Kalman R. E., 1960, Transactions of the ASME—Journal of Basic Engineering, **82**, 35
- Kasliwal V. P., Vogeley M. S., Richards G. T., Williams J., Carini M. T., 2015a, preprint, ([arXiv:1507.04251](https://arxiv.org/abs/1507.04251))
- Kasliwal V. P., Vogeley M. S., Richards G. T., 2015b, *MNRAS*, **451**, 4328
- Kelly B. C., Bechtold J., Siemiginowska A., 2009, *ApJ*, **698**, 895
- Kelly B. C., Sobolewska M., Siemiginowska A., 2011, *ApJ*, **730**, 52
- Kelly B. C., Becker A. C., Sobolewska M., Siemiginowska A., Uttley P., 2014, *ApJ*, **788**, 33
- Kinemuchi K., Barclay T., Fanelli M., Pepper J., Still M., Howell S. B., 2012, *PASP*, **124**, 963
- King A. R., Pringle J. E., West R. G., Livio M., 2004, *MNRAS*, **348**, 111
- King A. R., Pringle J. E., Livio M., 2007, *MNRAS*, **376**, 1740
- Kolodziejczak J. J., Caldwell D. A., Van Cleve J. E., Clarke B. D., Jenkins J. M., Cote M. T., Klaus T. C., Argabright V. S., 2010, in Society of Photo-Optical Instrumentation Engineers (SPIE) Conference Series. p. 1, doi:[10.1117/12.857637](https://doi.org/10.1117/12.857637)
- Koratkar A., Blaes O., 1999, *PASP*, **111**, 1
- Koratkar A. P., Gaskell C. M., 1991, *ApJS*, **75**, 719
- Kozłowski S., et al., 2010, *ApJ*, **708**, 927
- Krolik J. H., Horne K., Kallman T. R., Malkan M. A., Edelson R. A., Kriss G. A., 1991, *ApJ*, **371**, 541
- Lasota J.-P., 2001, *New Astron. Rev.*, **45**, 449
- Livio M., Pringle J. E., King A. R., 2003, *ApJ*, **593**, 184

- Lyubarskii Y. E., 1997, MNRAS, **292**, 679
- Maccarone T. J., 2014, in Maurizio F., Belloni T., Casella P., Gilfanov M., Jonker P., King A., eds, Space Sciences Series of ISSI, Vol. 49, *The Physics of Accretion onto Black Holes*. Springer, Chapt. 6, pp 101–120
- Mayer M., Pringle J. E., 2006, MNRAS, **368**, 379
- McClintock J. E., Horne K., Remillard R. A., 1995, ApJ, **442**, 358
- McHardy I. M., Papadakis I. E., Uttley P., Page M. J., Mason K. O., 2004, MNRAS, **348**, 783
- Mellen R. H., 1952, J. Acoust. Soc. Am., **24**, 478
- Misra R., Zdziarski A. A., 2008, MNRAS, **387**, 915
- Miyamoto S., Kitamoto S., Mitsuda K., Dotani T., 1988, Nature, **336**, 450
- Mościbrodzka M., Gammie C. F., Dolence J. C., Shiokawa H., Leung P. K., 2009, ApJ, **706**, 497
- Mushotzky R. F., Edelson R., Baumgartner W., Gandhi P., 2011, ApJ, **743**, L12
- Narayan R., Yi I., 1994, ApJ, **428**, L13
- Narayan R., Yi I., 1995a, ApJ, **444**, 231
- Narayan R., Yi I., 1995b, ApJ, **452**, 710
- Noble S. C., Krolik J. H., 2009, ApJ, **703**, 964
- O'Neill S. M., Reynolds C. S., Miller M. C., 2009, ApJ, **693**, 1100
- O'Neill S. M., Reynolds C. S., Miller M. C., Sorathia K. A., 2011, ApJ, **736**, 107
- Øksendal B., 2014, *Stochastic Differential Equations: An Introduction with Applications*, 6 edn. Universitext, Springer
- Pandit S. M., Wu S.-M., 2001, *Time Series and System Analysis With Applications*. Krieger Pub Co.
- Peterson Bradley M., 1997, *An Introduction to Active Galactic Nuclei*. Cambridge University Press
- Poutanen J., Fabian A. C., 1999, MNRAS, **306**, L31
- Pringle J. E., 1981, ARA&A, **19**, 137
- Rees M. J., 1984, ARA&A, **22**, 471
- Revalski M., Nowak D., Wiita P. J., Wehrle A. E., Unwin S. C., 2014, ApJ, **785**, 60
- Reynolds C. S., Miller M. C., 2009, ApJ, **692**, 869
- Rybicki G. B., Press W. H., 1992, ApJ, **398**, 169
- Rybicki G. B., Press W. H., 1995, Physical Review Letters, **74**, 1060
- Scargle J. D., 1981, ApJS, **45**, 1
- Schnittman J. D., Krolik J. H., 2013, ApJ, **777**, 11
- Schnittman J. D., Krolik J. H., Hawley J. F., 2006, ApJ, **651**, 1031
- Schnittman J. D., Krolik J. H., Noble S. C., 2013, ApJ, **769**, 156
- Sergeev S. G., Doroshenko V. T., Golubinsky Y. V., Merkulova N. I., Sergeeva E. A., 2005, ApJ, **622**, 129
- Shakura N. I., Sunyaev R. A., 1973, A&A, **24**, 337
- Simon D., 2006, *Optimal State Estimation: Kalman, H Infinity, and Nonlinear Approaches*. Wiley-Interscience
- Smith J. C., et al., 2012, PASP, **124**, 1000
- Starling R. L. C., Siemiginowska A., Uttley P., Soria R., 2004, MNRAS, **347**, 67
- Stengel Robert F., 1994, *Optimal Control and Estimation*. Dover Books on Mathematics, Dover Publications
- Stumpe M. C., et al., 2012, PASP, **124**, 985
- Thompson S. E., et al., 2015, Technical Report KSCI-19064-001, Kepler Data Release 24 Notes. National Aeronautics and Space Administration, NASA Ames Research Center, Moffett Field, California
- Titarchuk L., Shaposhnikov N., Arefiev V., 2007, ApJ, **660**, 556
- Ulrich M.-H., Maraschi L., Urry C. M., 1997, ARA&A, **35**, 445
- Uttley P., Casella P., 2014, in Maurizio F., Belloni T., Casella P., Gilfanov M., Jonker P., King A., eds, Space Sciences Series of ISSI, Vol. 49, *The Physics of Accretion onto Black Holes*. Springer, Chapt. 21, pp 453–476
- Uttley P., McHardy I. M., Papadakis I. E., 2002, MNRAS, **332**, 231
- Uttley P., Edelson R., McHardy I. M., Peterson B. M., Markowitz A., 2003, ApJ, **584**, L53
- Van Cleve J. E., Caldwell D. A., 2009, Technical Report KSCI-19033, Kepler Instrument Handbook. National Aeronautics and Space Administration, NASA Ames Research Center, Moffett Field, California
- Vaughan S., Fabian A. C., 2004, MNRAS, **348**, 1415
- Veledina A., Poutanen J., Vurm I., 2013, MNRAS, **430**, 3196
- Wanders I., et al., 1997, ApJS, **113**, 69
- Wehrle A. E., Wiita P. J., Unwin S. C., Di Lorenzo P., Revalski M., Silano D., Sprague D., 2013, ApJ, **773**, 89
- Wiberg Donald M., 1971, Schaum's Outline of Theory and Problems of State Space and Linear Systems. McGraw-Hill
- Williams J., Carini M. T., 2015, in American Astronomical Society Meeting Abstracts. p. #144.56
- Wood K. S., Titarchuk L., Ray P. S., Wolff M. T., Lovellette M. N., Bandyopadhyay R. M., 2001, ApJ, **563**, 246

This paper has been typeset from a TeX/LaTeX file prepared by the author.